CALIFORNIA STATE UNIVERSITY, NORTHRIDGE

The Effects of Quartz Dauphiné Twinning on Strain Localization in Polymineralic Rocks in a Mid-Crustal Shear Zone, Fiordland, New Zealand.

A thesis submitted in partial fulfilment of the requirements

For the degree of Master of Science in Geology

By

Courtney McGinn

August 2018

The thesis of Courtney McGinn is approved:

_____	_____
Dr. John Platt	Date
_____	_____
Dr. Josh Schwarz	Date
_____	_____
Dr. Elena Miranda, Chair	Date

California State University, Northridge

Acknowledgments

Funding for this project was provided by NSF award #EAR 1650219 to Miranda, and the CSUN Dept. of Geological Sciences Hanna Summer Student Research Award, Hanna Fellowship, and Larry Collins Scholarship to McGinn. We thank Andrew Cross and Zachary Michels for assistance with the MTEX scripts. We thank the New Zealand Department of Land Conservation for permission to sample in Fiordland and GNS for access to facilities to process our samples. We thank Zhan Peng for his assistance in the SEM Lab at CSUN. All data used in this manuscript are available upon request from the authors.

Table of Contents

List of Figures

Abstract

The Effects of Quartz Dauphiné Twinning on Strain Localization in Polymineralic Rocks in a Mid-Crustal Shear Zone- Fiordland, New Zealand.

By

Courtney McGinn

Master of Science in Geology

We use microstructural, electron backscatter diffraction (EBSD), crystal vorticity axis (CVA), and misorientation analyses to evaluate the effects of quartz Dauphiné twinning on strain localization processes within naturally deformed quartz and use recrystallized plagioclase for paleopiezometry calculations. The samples come from a mid-crustal shear zone exposed along the north shore of South Fiord in Lake Te Anau that lies along strike to the north of the Grebe Mylonite Zone (GMZ). We present results from two mylonite samples that deformed under amphibolite facies conditions, a garnet-bearing muscovite tonalite and a biotite granodiorite. A dramatic difference in Dauphiné twin development, exists in the quartz within the two mylonites, which we label as the untwinned quartz sample and Dauphiné-twinned quartz sample, respectively. We focus predominantly on the latter as it shows the best development of Dauphiné twins. In both samples, EBSD analysis reveals dynamic recrystallization (DRX) of quartz. Quartz grains have lobate grain boundaries and low intra-grain crystal plasticity indicative of grain boundary migration (GBM) DRX. Lineation measurements indicate an inclined-transpressional shear zone. CVA analysis reveals changes in the deformation, showing a

transition from simple shear- to pure shear-dominated deformation, that indicates a switch of the vorticity axis. Muscovite and biotite have similar patterns in both samples suggesting similar behavior of these minerals within the shear zone. Quartz CVA patterns are dramatically different between the samples, indicating that the 3D deformation geometry promotes different behavior of quartz in these otherwise similar samples. Cross-cutting relationships reveal that the Dauphiné-twinned grains are older than the nearly-untwinned grains. We correlate the CVA patterns of the Dauphiné-twinned grains and the nearly-untwinned grains with simple shear-dominated and pure shear-dominated deformation, respectively, and use this information to display the pole figures in the correct reference frame. Pole figures and misorientation analysis reveal patterns that are consistent with the activation of known high-temperature slip systems, particularly in the nearly-untwinned grain population, while both low- and high-temperature slip systems are preserved in the Dauphiné-twinned grains. The activity of low-temperature slip systems in the Dauphiné-twinned grains results in the grains being less deformable for high-temperature slip compared to the nearly-untwinned grains. The stress calculated from the recrystallized plagioclase grains using the Twiss (1977) piezometer provide a value of 53.8-59.7 MPa. We conclude that Dauphiné twinning reduced grain sizes and helped to initially localize strain caused by deformation in an inclined-transpressional shear zone. Dauphiné twins developed during the onset of deformation and preferentially orientated the grains, resulting in strain localization. The nearly-untwinned quartz grains recorded the change in the deformation due to the grains being more deformable and GBM DRX swept grain boundaries through the grain. Dauphiné-twinned grains were less deformable, therefore the older deformation was preserved as GBM DRX maintained the low intra-grain strain. The higher grain orientation spread (GOS) value of the *z*-twin compared to the *r*-twin, as well as the higher GOS value of the Dauphiné-twinned grains compared to the nearly-untwinned grains, drove the mobility of lower-strain grains into higher-strain grains. The mobility of grains acted to reduce strain and maintain localization of the shear zone.

Chapter 1: Introduction

High temperature quartz deformation is rarely preserved in naturally deformed rocks (e.g. Stipp et al., 2002), though many experimental studies exist on this topic (Hirth and Tullis, 1992; Stipp and Tullis, 2003; Stipp et al., 2010; Cross et al., 2017). In addition, few studies exist that investigate how Dauphiné twins affect dynamic recrystallization (DRX) at high temperatures (>600º C) (Tullis and Tullis, 1972; Tullis et al., 1973; Mainprice et al., 1986; Pehl and Wenk, 2005; Piazolo et al., 2005). Dauphiné twinning, described as a 180º rotation about the *c*-axis (Thomas and Wooster, 1951; Tullis and Tullis, 1972; Rahl et al., 2018), allows the positive and negative rhombs and <*a*> directions to be exchanged without changing [*c*] (Thomas and Wooster, 1951; Tullis and Tullis, 1972; Rahl et al., 2018). Natural and experimental studies both conclude that Dauphiné twinning allows large strains to be accommodated due to the twins' ability to switch between the positive and negative <*a*> directions (Lloyd, 2004; Menegon et al., 2011; Pehl and Wenk, 2005; Wenk et al., 2006, 2007; Morales et al., 2014). Furthermore, quartz has anisotropic elastic properties resulting in the pole to the *z*-plane being twice as stiff as the *r*-plane (Wenk et al., 2009; Rahl et al., 2018). This results in a competence contrast between the more deformable *r*-twin and less deformable *z*-twin, with the *r*-twin bands being the preferred site for dynamic recrystallization (Menegon et al., 2011). Studies of naturally deformed rocks have mainly focused on Dauphiné twinning in rocks that underwent subgrain rotation (SGR) dynamic recrystallization (Lloyd, 2004; Menegon et al., 2011; Morales et al., 2015). The interaction between Dauphiné twins and grain boundary migration (GBM) in quartz is an under-studied occurrence in naturally

deformed rocks (Neumann, 2000; Piazolo et al., 2005) that could play a significant role in how strain localizes and is maintained in shear zones in the middle to lower crust.

In this study, we investigate the role of Dauphiné twins in strain localization processes at high temperatures where microstructures are consistent with GBM DRX. We build on the work of Menegon et al. (2011) by analyzing samples that have deformed via GBM, and we build on the work of Neumann (2000) and Piazolo et al. (2005) by further exploring the relative timing of twin development and their effect on rock texture. Fiordland, New Zealand provides an ideal location to investigate such deformation due to the presence of a network of exhumed middle- to lower-crustal shear zones (Klepeis et al., 2004; Scott et al., 2011; Schwartz et al., 2017) that are along strike to each other (Marcotte et al., 2005; Allibone et al., 2009; Scott, 2013). These zones provide the opportunity to analyze how deformation processes vary with crustal depth. We specifically analyze samples from a shear zone exposed on the north shore of South Fiord in Lake Te Anau. This shear zone is north of and along-strike to the Grebe Mylonite Zone (GMZ) (Allibone et al., 2009), a mid-crustal shear zone in this network (Scott et al., 2009, 2011; Scott, 2013; Schwartz et al., 2017).

We analyze two representative mylonites with a dramatic difference in the Dauphiné twin development. One sample has prevalent Dauphiné twinning while the other is nearly-untwinned, which we label as the Dauphiné-twinned quartz sample and the untwinned quartz sample, respectively. These two samples provide a comparison of the role that Dauphiné twinning plays in strain localization. We hypothesize that Dauphiné twinning initially helped strain localization processes, but that the Dauphiné twins became less deformable over time, which prevented the grains from recording the

changes in deformation. We discuss the role of the Dauphiné twins as initial sites for dynamic recrystallization. We hypothesize that the *z*-twins were less able to accommodate the changes in deformation than the more deformable *r*-twin as a result of the active slip systems. We calculate stress based on recrystallized plagioclase using the Twiss (1977) piezometer to estimate deformation conditions.

Chapter 2: Geologic Background

During the Early Cretaceous, New Zealand was part of the convergent boundary along eastern Gondwanaland, and subduction produced a narrow belt of magmatism forming the Median Batholith (Mortimer et al., 1999). The median batholith was built in two installments, forming the inboard and outboard arc rocks (Allibone et al., 2009; Schwartz et al., 2017). Crustal-scale shear zones developed near the boundary between the outboard (Carboniferous-Early Cretaceous) and inboard (Early to Late Cretaceous) Median Batholith (Scott et al., 2011). The Indecision Creek Shear Zone forms the lower crustal part of this boundary (Klepeis et al., 2004; Marcotte et al., 2005) and the Grebe Mylonite Zone (GMZ) developed in the middle crust under amphibolite conditions and was active from 128-116 Ma (Scott et al., 2011) during a period of contraction and transpression (Marcotte et al., 2005; Scott et al., 2011; Klepeis et al., 2016) . The GMZ is developed within rocks such as the Darran Suite (230-136 Ma). The Darran Suite is composed of multiple bodies including the Hunter and Murchison Intrusives (Allibone et al., 2009; Scott et al., 2011). Both units are compositionally and texturally heterogeneous, ranging from gabbro to granite and undeformed to foliated, respectively (Allibone et al., 2009), containing small, Carboniferous-aged plutons along strike of the GMZ (Rattenbury and Isaac, 2012).

The samples used in this study were collected from a mid-crustal shear zone exposed along the north shore of South Fiord in Lake Te Anau that lies along strike to the north of the GMZ (Fig. 1). The distributed shear zone (~5 km) is contained within and separates the Hunter and Murchison Intrusives, containing high-strain zones that grade from mylonite to ultramylonite (laterally continuous for 3-15 m). Mylonitic foliations in

the shear zone primarily strike SW and dip moderately to steeply NW with lineations plunging shallowly towards the S-SW that steepen from west to east in the shear zone. We have selected two samples from this shear zone that best characterize the high-strain fabric development and display differences in the relative amount of Dauphiné twinning. These samples come from either side of the contact between the Hunter and Murchison Intrusives, and we target these for microstructural and electron backscatter diffraction (EBSD) analysis.

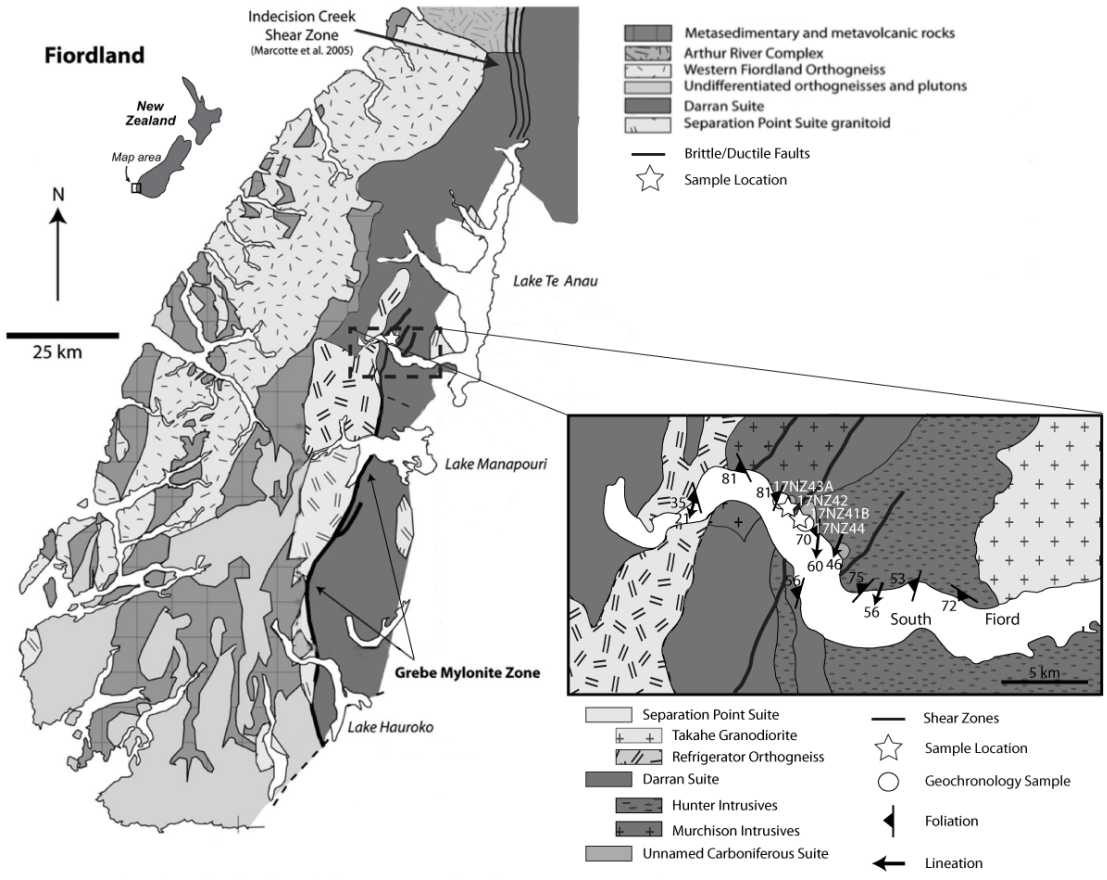

Fig. 1. Simplified geologic map of Fiordland, New Zealand modified after Scott et al. (2011), Rattenbury and Isaac (2012), Klepeis et al. (2016), and Buritica (2018). The dashed box encompasses the extent of field work for this study. The white stars indicate the location of samples used in this study and the white circles indicate geochronology samples used to constrain the age of the local geology.

A garnet-bearing muscovite tonalite (17NZ41B) and a biotite granodiorite (17NZ42), which we call the untwinned quartz sample and Dauphiné-twinned quartz sample, respectively, (see Supplemental Fig. SP1 for hand sample photos) were collected from well-foliated rocks. S-C fabric development shows predominantly sinistral shear sense indicators in plagioclase indicating top-to-the-NE sense of shear. The untwinned quartz sample is contained within an unnamed Carboniferous suite (Buritica, 2018) (Fig. 1), and has a mylonitic fabric oriented at 185º, 70º NW and a lineation of 19º/186º SW. A nearby sample (17NZ44) with similar mineralogy and textures yielded a U-Pb zircon age of 341.0±4.8 Ma (Buritica, 2018). The Dauphiné-twinned quartz sample, also contained within the unnamed Carboniferous suite (Buritica, 2018), has a mylonitic fabric oriented at 201º, 81º NW; this sample has a U-Pb zircon age of 354.3±7.8 Ma (Ringwood, 2018). A nearby sample (17NZ43A) has a U-Pb zircon age of 344.0±7.6 Ma (Ringwood, 2018), and titanite aligned with the mylonitic fabric of this nearby sample provided a U-Pb age of 123.2±9.4 Ma and a Zr in titanite temperature of 608±12 ºC (Buritica, 2018). Samples from two different units were selected to compare the microstructural development and strain localization processes. Both samples were cut perpendicular to the foliation and parallel to the lineation for microstructural and EBSD analysis.

Chapter 3: Methods

3.1 Light microscopy

The mineral phases and deformation microstructures were identified using a Nikon Eclipse 50iPol polarizing microscope and a Leica MZ8 macroscope. After a thorough analysis of each sample utilizing plane and cross-polarized light, locations were selected for further microstructural analysis via EBSD to capture the deformation in quartz.

3.2 EBSD

EBSD data were collected at California State University- Northridge using a FEI Quanta 600 scanning electron microscope (SEM) equipped with an Oxford Instruments Nordlys EBSD detector and AZtec EBSD acquisition software. Ultra-polished samples were analyzed under low vacuum conditions (20 Pa water). Beam maps were generated to characterize the deformation microstructures and determine the crystallographic orientation of grains. For this study, we constructed two EBSD maps from two samples (an untwinned quartz and Dauphiné-twinned quartz sample), focusing on the recrystallized quartz bands. The working conditions are shown in Table 1 for each map.

Sample	Sample Type	Size (mm^2)	Step Size (μm)	Accelerating Voltage (kV)	Spot Size	Filament Current (A)	Emission Current (μA)	Wokring Distance (mm)	Raw Indexing Rates of EBSD map (%)
Untwinned Quartz Sample (17NZ41B)	Quartz Band (stitched)	6.82	2.50	20-25	6.4-6.9	2.31-2.72	92-101	13.5-14.3	98.2-99.0
Dauphiné-twinned Quartz Sample (17NZ42)	Quartz band with plagioclase lens (stitched)	22.70	3.70	25-30	6.4-7.1	2.28-2.71	93-108	14.8-15.4	97.6-99.8

Table 1: Working conditions during data collection for the EBSD maps.

We used the Oxford Instruments hkl Channel 5 software suite to process the EBSD data. Data were noise reduced by 1) removal of wild spikes and 2) extrapolating

zero solutions to match the orientation of 8 or 7 neighbor pixels of the same phase. Maps were generated using the hkl Channel 5 Tango software. In all maps, the grain boundaries are defined as having ≥10º of misorientation and the subgrain boundaries as having between 2-10º of misorientation. Dauphiné twins are identified by a 60º ±5º rotation around the *c*-axis (Lloyd, 2004; Stipp and Kunze, 2008; Menegon et al., 2011) where the twin is defined as the *r*-twin and the host is defined as the *z*-twin (Menegon et al., 2011). Mineral distribution is shown on the phase maps and spatial distributions of grain orientations are shown on the inverse pole figure (IPF-X) maps to show crystal orientation relative to the stretching lineation. Grain orientation spread (GOS) maps compare the orientation of each pixel in the grain to the overall orientation of the grain to use as a proxy for total strain in a crystal. Local misorientation maps are then used to identify low angle (<3º) misorientations in the grains. Schmid factor maps measure how well the quartz grains are oriented for slip along known slip systems and if grains are in "soft" or "hard" orientations for slip in the specified slip system. In the Schmid factor maps, we assume σ_1 is oriented 45º from the trace of the foliation to maximize the shear stress component along slip planes. Therefore, maps were generated using an alpha angle of 45º, and grains in soft orientations have planes oriented 45º to the applied stress.

The MTEX toolbox for MATLAB (Bachmann et al., 2011) was used to plot the data gathered from the EBSD analysis to determine the shear zone kinematics and characterize the crystallographic preferred orientation (CPO). Crystallographic vorticity axis (CVA) analysis provides information on the kinematics of crystal-plastic deformation independent from the lineation and foliation measurements. Analysis was completed for both the untwinned and Dauphiné-twinned sample focusing on the bulk

sample (all minerals together) and separate subsets of micas and quartz. This was done by using the open-source code for CVA analysis available on GitHub (https://github.com/zmichels/CVA) developed by Michels et al. (2015) that uses rotation statistics to calculate the dispersion axis from crystallographic orientations within a grain. Crystallographic orientation data for quartz to determine CPO were plotted in lower hemisphere, equal area stereographic projection pole figures using one point per grain to prevent oversampling of large grains and calculated using an Orientation Distribution Function (ODF) and a half width of 10º. The contour density of crystallographic orientations is indicated by multiples of uniform distribution (m.u.d). CPO is plotted in kinematic reference frame or vorticity normal reference frame for two subsets based on the CVA and Schmid factor map interpretations (Giorgis et al., 2016). MTEX was used to measure the fabric strength in the pole figures using the M-index (Skemer et al., 2005) and the J-index (Bunge, 1982).

Misorientation axes are plotted to aid in the identification of deformation mechanisms in quartz utilizing MTEX. A histogram shows the frequency of occurrence plotted against the angle of misorientation measured in degrees (binned into 5º increments) with a minimum of a 3º misorientation angle to minimize low-angle errors (Prior et al., 1999). Low-angle misorientations (3-10º) have two distinct populations from 3-5º and 5-10º and were split out to compare misorientation development. The orientation of misorientation axes are plotted in the crystal reference frame. Subsets composed of two reference grains in a soft orientation for prism <*a*> slip were selected for a comparison misorientation analysis. Grains with Dauphiné twins were subsetted to determine how twinning affected deformation and to compare the *r*-twin to the *z*-twin.

Chapter 4: Results

4.1 Untwinned quartz sample (17NZ41B) microstructures

4.1.1 Microstructures from light microscopy

Light microscopy reveals the development of deformation microstructures in plagioclase and quartz. Fine-grained plagioclase (45%) and coarser-grained quartz (35%) are separated into bands (Fig. 2a) within an S-C mylonite (see supplemental Fig. SP2) where the muscovite that has minorly altered to chlorite is associated with the C-shears, and the slightly coarser quartz grains are associated with domains exhibiting the S-fabric. Muscovite and chlorite form anastomosing bands, separating the plagioclase and quartz bands, containing grains at variable orientations to foliation (Fig. 2b). Fine-grained plagioclase (average grain diameter <20 μm) grain boundaries are pinned by muscovite grains (Fig. 2c). Rare plagioclase porphyroclasts are fairly altered to sericite (Fig. 2d), but are shown to exhibit undulose extinction and local subgrain development, with fine-grained plagioclase present along rims. Quartz bands are nearly monomineralic and composed of completely recrystallized grains that range from fine to coarse-grained (6-700 μm, ~115 μm average). Quartz grains exhibit GBM recrystallization microstructures including undulose extinction and limited subgrain development, and have grain boundaries that range in shape from lobate to straight. Quartz grain boundaries are pinned by minor inclusions of both calcite (Fig. 2e) and muscovite grains (Fig. 2f). A quartz-rich band within this S-C mylonite sample was selected for detailed EBSD analysis (Fig. 2a).

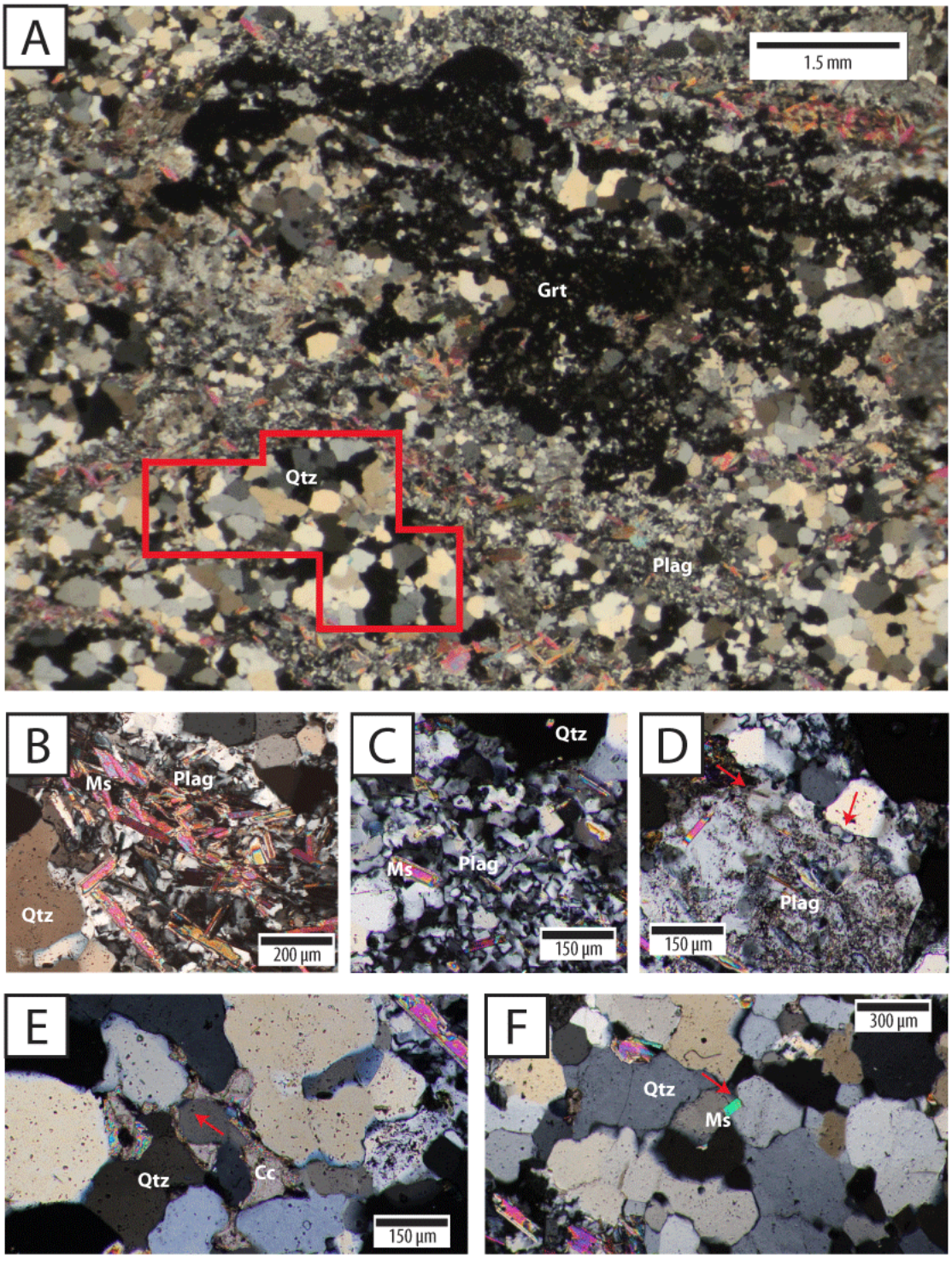

Fig. 2. Photomicrographs of the untwinned quartz sample in cross-polarized light. a) Characteristic banding of quartz and plagioclase with the location of the EBSD map outlined in red. b) Muscovite in variable orientations separating plagioclase and quartz. c) Recrystallized plagioclase pinned by muscovite. d) Altered plagioclase porphyroclast with subgrains (red arrows). e) Quartz grains pinned by calcite (red arrow). f) Quartz grains pinned by muscovite (red arrow). Qtz=quartz, Plag=plagioclase, Grt=Garnet, Ms=Muscovite Cc=Calcite

4.1.2 EBSD data from the untwinned quartz sample

EBSD analyses confirm the GBM DRX microstructures observed with light microscopy, and reveal the presence of minor Dauphiné twinning in the quartz. Plagioclase, calcite, and muscovite (Fig 3a) form pinning microstructures in quartz. Though there is no overall dominant orientation of quartz grains, there are clusters of similarly-oriented grains separated by a few interstitial grains of different orientations termed 'island grains' in Stipp et al. (2002) (Fig. 3b). Rare subgrains are most common within the coarser, lobate-shaped grains (Fig. 3b). The IPF-X maps show that the Dauphiné-twinned grains have twins that range in color from pink to purple, indicating that the twins are oriented with their *r*-pole parallel to the lineation. The untwinned portions of these grains range in color from orange to green, which correlates with having their *z*-poles parallel to the lineation. The quartz GOS map (Fig. 3c) reveals an overall low amount of intra-grain crystal plasticity in the grains. The few grains with higher GOS values tend to have more subgrain development in contrast to the other grains.

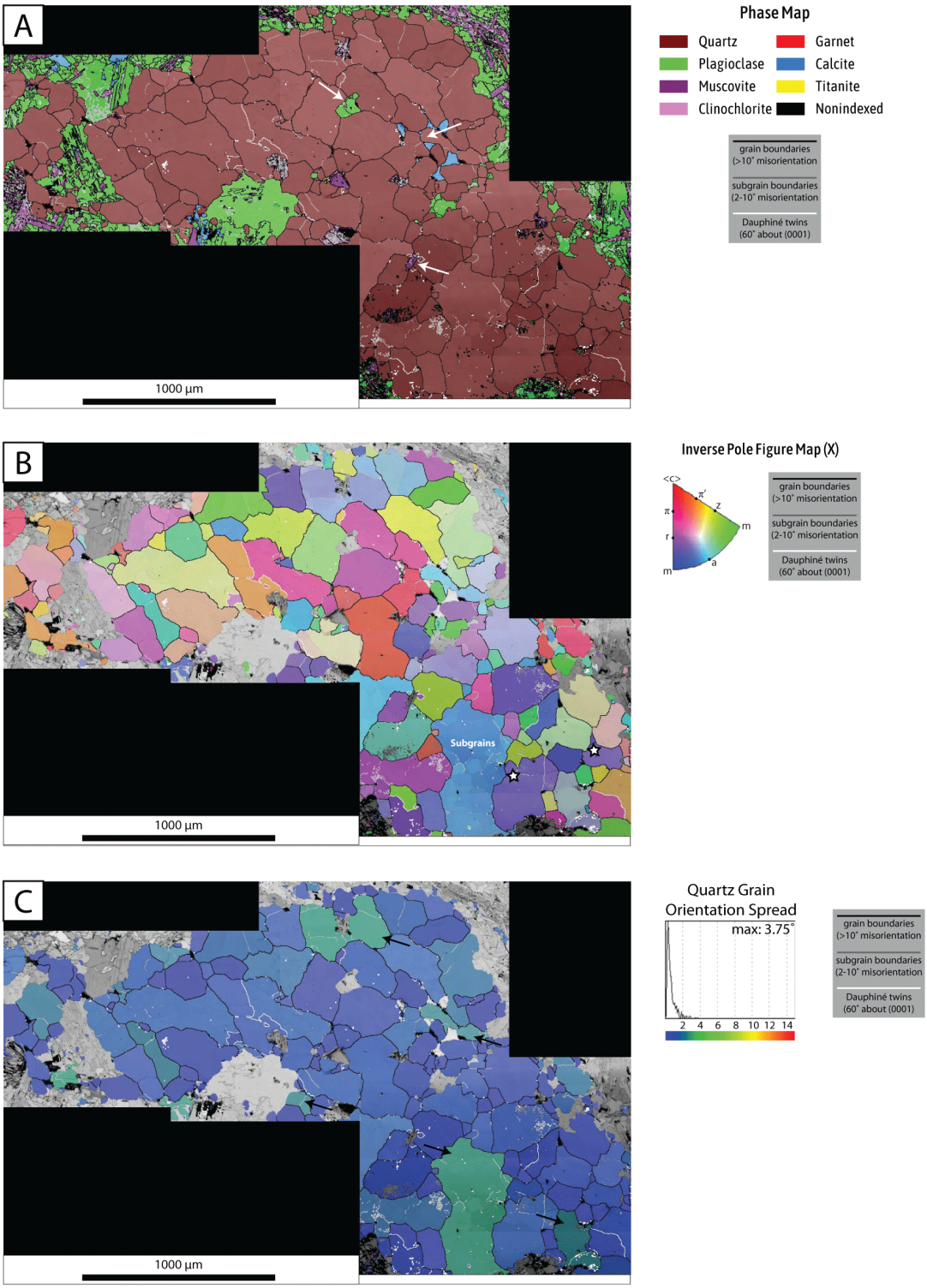

Fig. 3. EBSD maps of a quartz band in the untwinned quartz sample. a) White arrows in the phase map highlight pinning microstructures in quartz due to minor calcite, plagioclase, and muscovite. b) The IPF-X map highlights the presence of minor Dauphiné twinning and rare subgrains. White stars indicate examples of island grains. c) The GOS map shows overall low intra-grain crystal plasticity, and the grains with a relatively higher GOS value (black arrows) contain subgrains.

4.2 Dauphiné-twinned quartz sample (17NZ42) microstructures

4.2.1 Microstructures from light microscopy

Light microscopy analysis of plagioclase and quartz shows extensive recrystallization of both minerals. The quartz (35%) and plagioclase (50%) bands (Fig. 4a) are separated by bands of biotite and minor muscovite (15%) that contain grains oriented parallel and oblique to foliation (Fig. 4b). The quartz domains align with the S-shears and the biotite and muscovite domains align with the C-shears in the fabric (see supplemental Fig. SP3). Plagioclase is fine-grained (~50 μm average diameter), and within the plagioclase-rich domains, the fine grains are pinned by interstitial quartz and biotite (Fig. 4c). Plagioclase porphyroclasts are not common (see supplemental Fig. SP3), but porphyroclast-shaped domains of recrystallized plagioclase are present (Fig. 4d). In contrast, the recrystallized quartz is fairly coarse-grained compared to plagioclase, but with highly variable grain sizes (9-1000 μm, ~230 μm average). The quartz grains commonly show distinctive microstructures of GBM recrystallization, including interpenetrating lobate grain boundaries, undulose extinction, some subgrain development, and grain boundary pinning by biotite (Fig. 4e), muscovite, and plagioclase (Fig. 4f). In addition, chessboard extinction patterns are observed (Fig. 4g). A recrystallized quartz band exhibiting these distinctive microstructures was targeted for EBSD analysis (Fig. 4a).

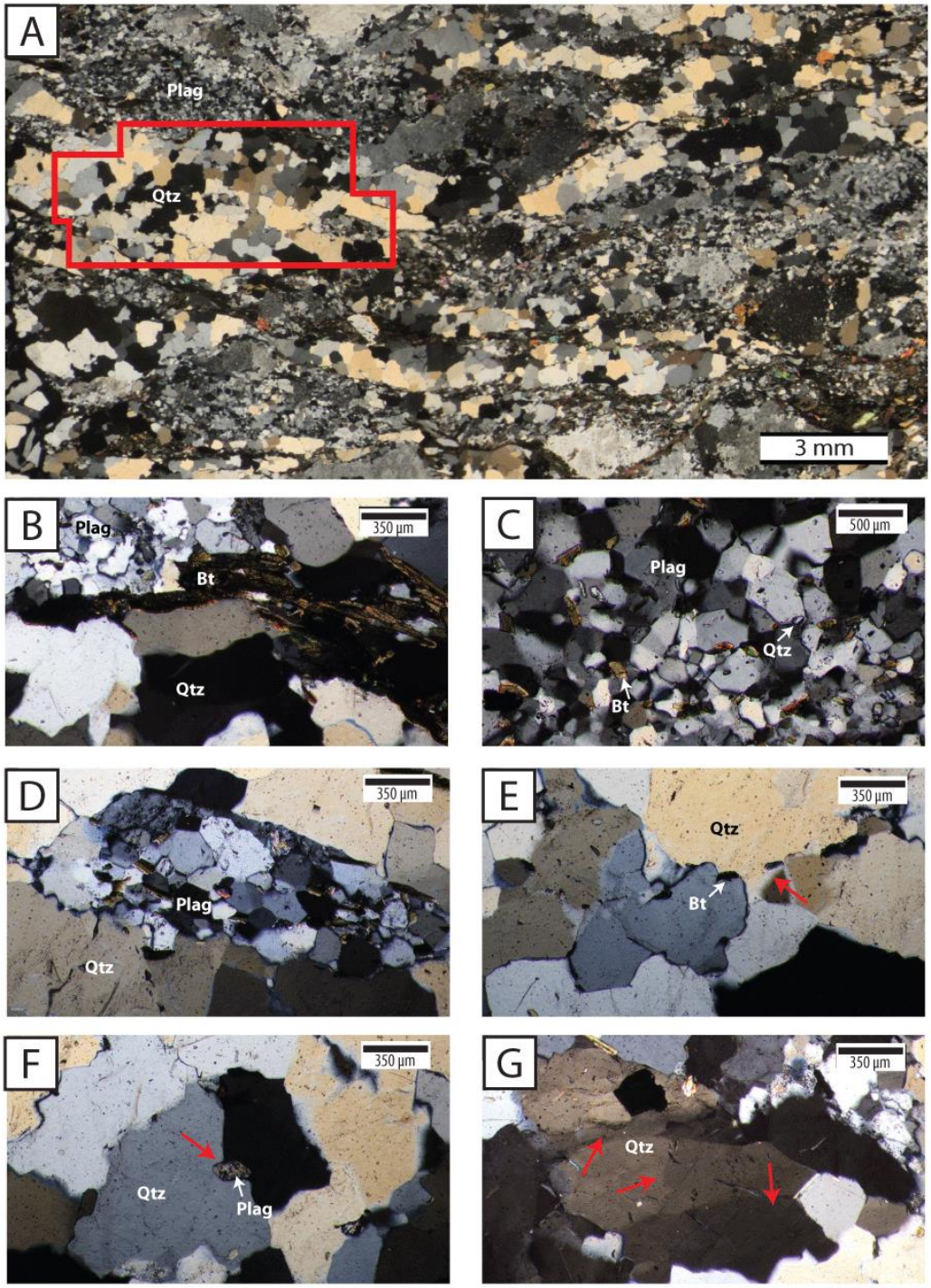

Fig. 4. Photomicrograph of the Dauphiné-twinned sample in cross-polarized light. a) Characteristic fabric with coarse-grained quartz and fine-grained plagioclase forming compositional bands. The red box indicates the area of EBSD analysis. b) Biotite with variable orientations at the interface between quartz- and plagioclase-rich bands. c) Fine-grained, recrystallized plagioclase pinned by muscovite and quartz. d) Porphyroclast-shaped region of recrystallized plagioclase grains that show undulose extinction and subgrain development. e) Quartz pinned by biotite (red arrow). f) Quartz pinned by altered plagioclase (red arrow). g) Quartz grain showing chessboard extinction and the development of subgrains (red arrows). Qtz=Quartz, Plag=Plagioclase, Bt=Biotite

4.2.2 EBSD data from the Dauphiné-twinned quartz sample

EBSD analysis confirms the optically observed GBM microstructures and reveals the presence of prevalent Dauphiné twinning. Plagioclase, biotite, and muscovite form pinning microstructures in quartz (Fig. 5a). The IPF-X map reveals 'island grains' (stars in Fig. 5b), and a dominant orientation of quartz grains in which the *z*- and *π*'-poles are parallel to the lineation. In quartz with Dauphiné twins, the twinned regions generally range from pink to indigo in color, indicating that the twins have the *π*-, *r*-, or *m*-poles parallel to the lineation. The non-twinned portions of these grains range from orange to green in color, indicating host grains have the *z*-, *m*-, or *π'*-poles parallel to the lineation (Fig. 5b). Grains with minor or absent twinning have convex lobes that protrude into the Dauphiné-twinned grains. The GOS map demonstrates that quartz has an overall low amount of intra-grain crystal plasticity, particularly in smaller grains (20-130 μm in diameter) that have minor or absent twinning (Fig. 5c). The *z*-twins have relatively higher GOS values compared to the *r*-twins, with the *z*-twins containing a higher density of subgrain walls (Fig. 5d). The local misorientation map shows that grains with fewer lower angle boundaries (i.e. grain indicated by white star in Figure 5d) have convex grain boundaries that protrude into grains with prevalent twinning (i.e. grain indicated by black star in Fig. 5d), and into other grains having a greater density of low-angle boundaries. The orientation of convex lobes indicated in Figure 5d are parallel to the twin boundaries in the grain indicated by the black star, with subgrain walls that cross-cut the twins.

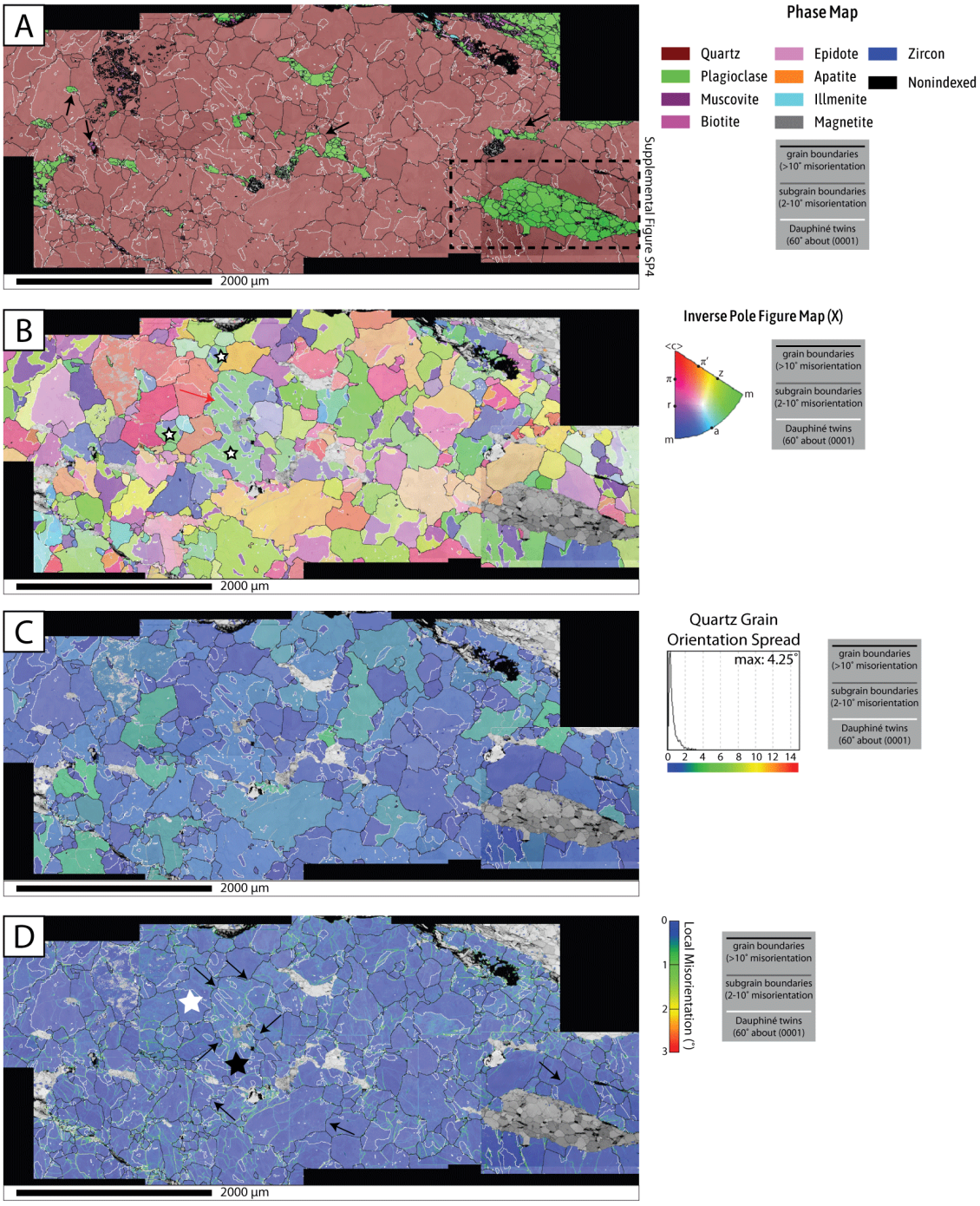

Fig. 5. EBSD maps of quartz band in the Dauphiné-twinned sample. a) The phase map shows pinning of quartz by plagioclase and biotite (black arrows). The plagioclase in the dashed box in (a) is focused on in the Supplemental Figure SP4. b) The IPF-X map shows island grains (white stars) and highlights the presence of Dauphiné twins and rare subgrains. c) The GOS map shows the overall low intra-grain crystal plasticity of quartz and the relatively higher GOS values of the *z*-twins to *r*-twins. d) The Local misorientation map reveals grains with fewer low angle misorientations forming convex lobes into grains with a higher density of misorientations indicated by arrows which parallel twin boundaries. The black and white star identify grains for further analysis.

4.3 Crystallographic vorticity axis analysis

Crystallographic vorticity axis (CVA) analysis for the untwinned quartz sample reveals distinct differences in the CVA geometry for the bulk sample and the individual minerals. For the untwinned quartz sample, the dispersion axes for the bulk sample (Fig. 6a) show a maximum between the Y- and Z- axes and a weaker set of maxima on the primitive that are oriented 40º clockwise from the lineation. The muscovite CVA plot (Fig. 6b) shows a spread of orientations along the primitive, where the center of the spread is oriented 40º clockwise from the lineation, similar to the weaker maxima in the bulk CVA plot. The quartz CVA (Fig. 6c) plot shows a broad girdle of vorticity axes roughly parallel to the foliation; within this girdle, there are two strong maxima located between the Y-axis and primitive circle.

CVA analysis for the Dauphiné-twinned quartz sample also shows differences in the CVA geometry for the bulk sample and the individual minerals, but the CVA geometry is also different compared to the untwinned quartz sample. The CVA bulk data plot (Fig. 6d) and the biotite CVA plot (Fig. 6e) both show maxima along the primitive circle oriented ~15º clockwise from the lineation. The quartz CVA plot (Fig. 6f) shows two sets of maxima that correlate with the Dauphiné-twinned and nearly-untwinned grain populations. One set is similar in orientation to the maxima in the biotite CVA plot, and is correlated with the nearly-untwinned grain population. The other set is associated with the Dauphiné-twinned grains and forms a faint girdle parallel to the Z-axis with two maxima on the primitive circle correlated to the *r*-twins and a higher density cluster near the Y-axis correlated to the host (*z*-twin).

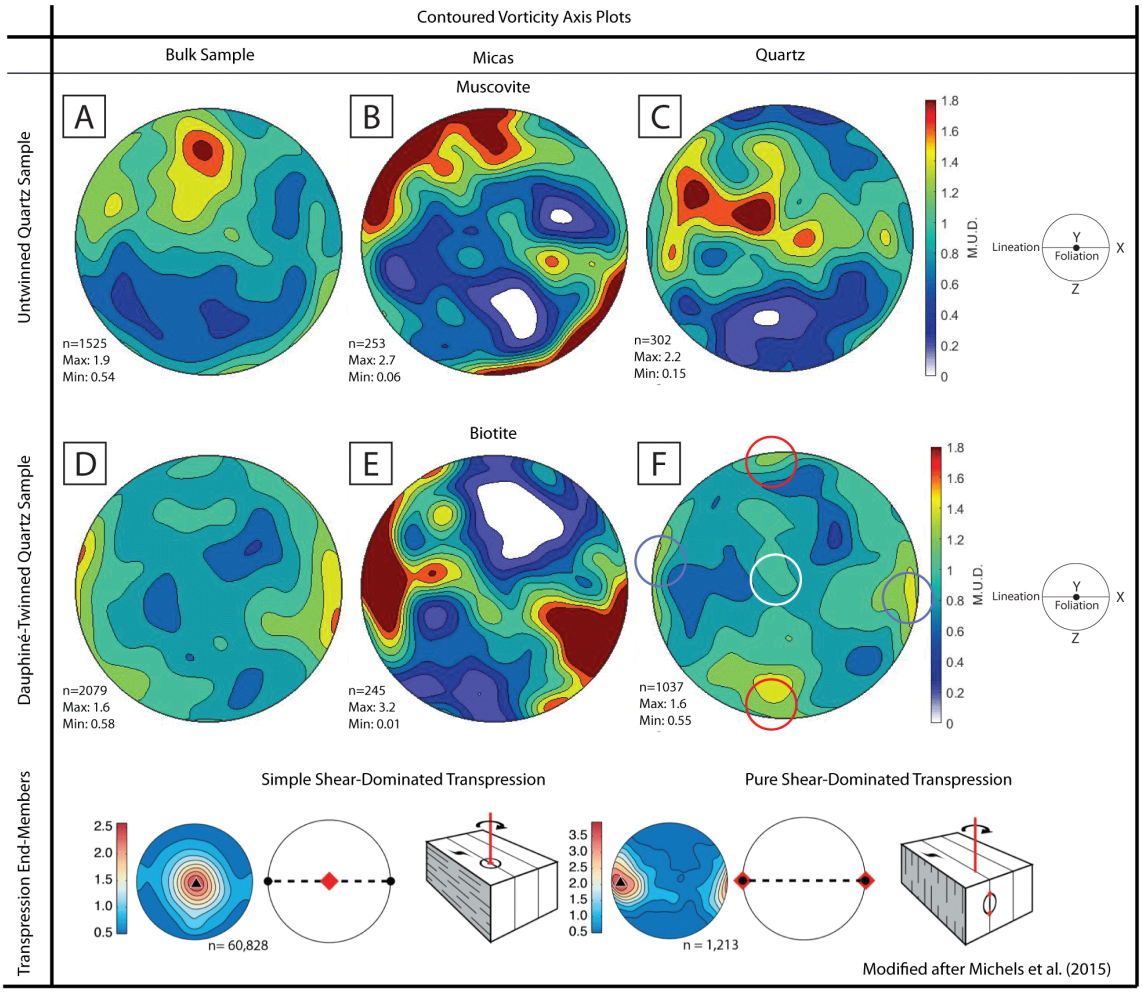

Fig. 6. Crystallographic vorticity axis (CVA) analysis of the untwinned and Dauphiné-twinned quartz sample. Contoured pole figures are equal area, lower hemisphere projections with a 10º contour half width. CVA analysis results for the untwinned quartz sample are displayed for (a) bulk sample and the individual minerals of (b) muscovite and (c) quartz. The Dauphiné-twinned quartz sample CVA data are displayed for (d) bulk sample and the individual minerals of (e) biotite and (f) quartz. In the quartz CVA of the Dauphiné-twinned quartz sample (f), four maxima on the primitive circle and a higher density cluster are indicated. The nearly-untwinned grains are associated with the maxima indicated by the blue circles. The Dauphiné-twinned grains are associated with the maxima indicated by the red circles (twinned portion) and the higher density cluster indicated by the white circle (host portion). A key modified after Michels et al. (2015) shows the CVA analysis for the end-members of simple-shear dominated transpression and coaxial-dominated transpression.

4.4 Quartz Schmid factor maps for the Dauphiné-twinned quartz sample

Schmid factor maps of the Dauphiné-twinned quartz sample reveal grain orientations ranging from soft (Schmid factor over >0.25) to hard (Schmid factor <0.25) for known slip systems (Fig. 7). The high proportion of blue grains in the basal <*a*> map

indicates that they are oriented unfavorably for this slip system (Fig. 7a). In the rhomb <*a*> map, the Dauphiné twinning is very apparent (Fig. 7b), and twins having their π- or *r*-pole parallel to the lineation (Fig. 5b) are in softer orientations for rhomb <*a*> slip compared to their untwinned hosts. The prism <a> map has the largest proportion of grains in a favorable orientation for slip, with a sizeable peak of values >0.4 (Fig. 7c). Two reference grains in a soft orientation for prism <*a*> slip were selected for further analysis. These grains, a nearly-untwinned grain indicated by a white star and a Dauphiné-twinned grain indicated by a black star, show distinct CVA patterns (see Fig. 6g), aligning with the maxima for the nearly-untwinned and Dauphiné-twinned grains, respectively. The prism [c] map is very similar to the basal <a> map (compare Fig. 7d and Fig. 7a), but many of the orange grains in the basal <a> map instead show red colors in the prism [c] map.

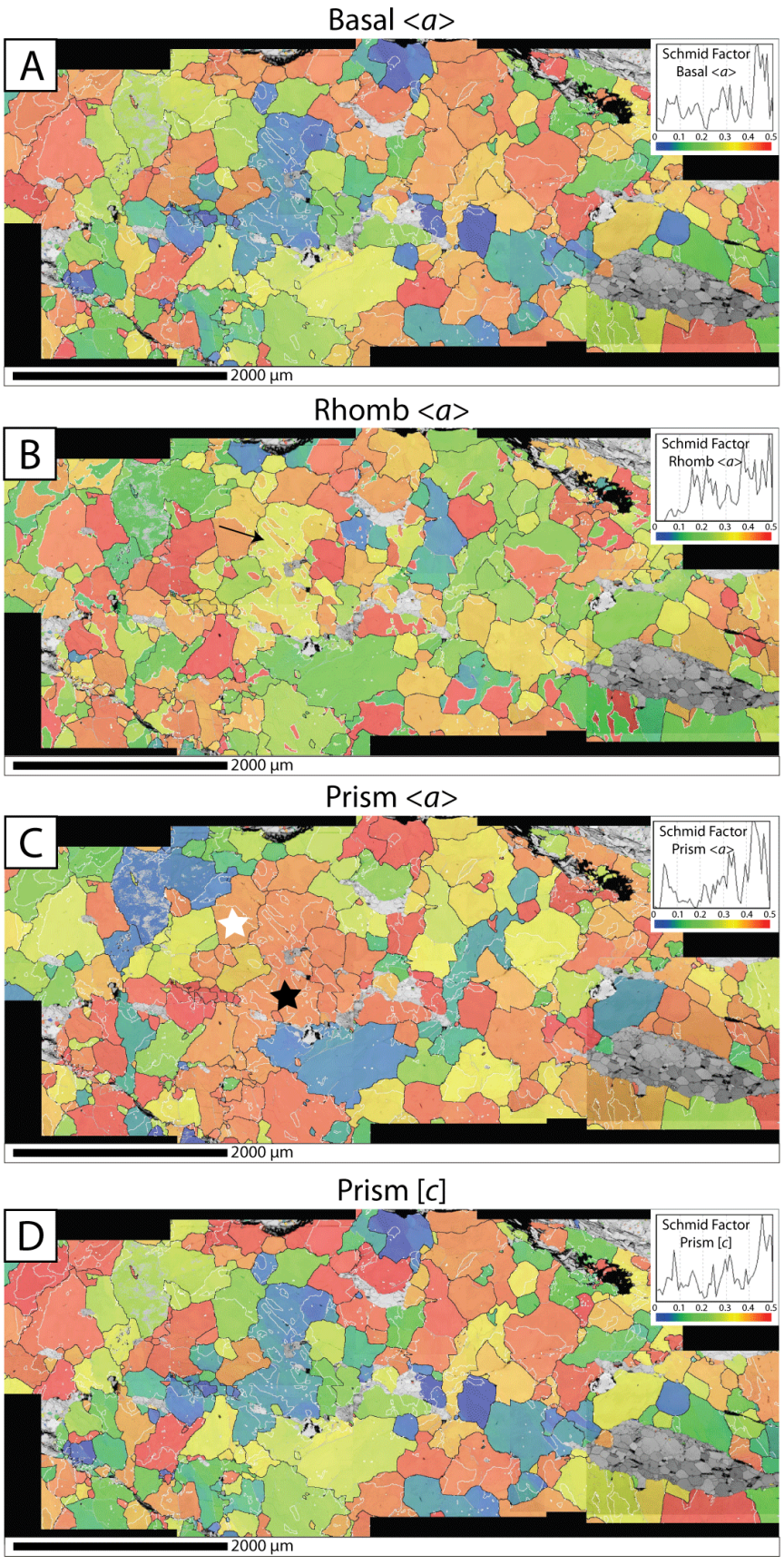

Fig. 7. Schmid factor maps of the quartz Dauphiné-twinned sample. Blue grains are oriented in a hard orientation for slip, whereas red grains are in a soft orientation for slip for a given slip system. a) Basal <*a*> slip. b) Rhomb <*a*> slip which shows that *r*-twins are in softer orientations than the host as observed in the grain indicated by the arrow. c) Prism <*a*> slip. The black and white star indicate two reference grains in a soft orientation for prism <*a*> slip that were used for further analysis. d) Prism [*c*] slip.

4.5 Quartz crystallographic orientation data for the Dauphiné-twinned quartz sample

Pole figure plots reveal a crystallographic preferred orientation (CPO) in quartz by the presence of a moderately strong, non-random bulk fabric (J-index 4.26, M-index 0.07). The *c*-axis plot showing all quartz grains in the kinematic reference frame (Fig. 8a) has a maximum off-center of the Y-axis, with some spread towards the primitive. Two weak maxima are located along the primitive circle, at about ~50º counterclockwise from the Z-axis; a weak maximum forms nearly parallel to the lineation. Orientations from two grains in soft orientations in the prism <*a*> Schmid map (Fig. 7c) plot in different

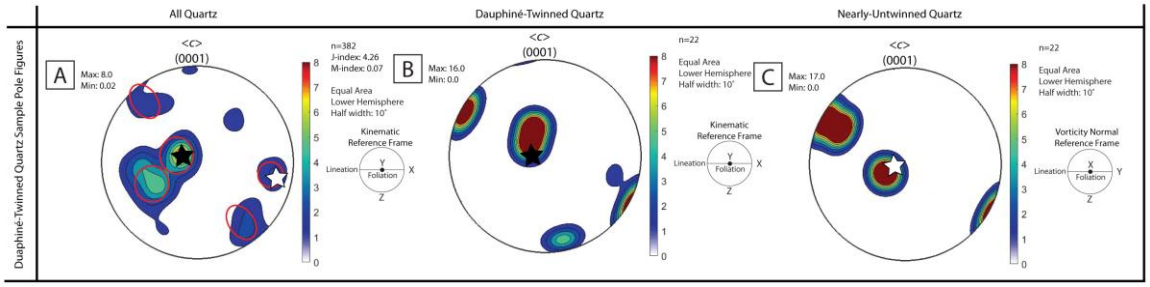

Fig. 8. Contoured pole figures of quartz crystallographic orientations in the Dauphiné-twinned quartz sample based on a one point per grain subset. Data are shown in the kinematic reference frame (a, b) and in the vorticity normal reference frame (c). a) Pole figure of quartz grain orientations from the EBSD map shown in Figure 5. The black star indicates orientation of the large, Dauphiné-twinned grain in the center of the prism <*a*> Schmid map, and the white star indicates the orientation of an adjacent, nearly-untwinned grain, with convex lobes that protrude into the Dauphiné-twinned grain. The two subsets have (b) Dauphiné-twinned grain orientations and (c) nearly-untwinned grain orientations have similar CPOs. See Supplemental Figure SP5 for the grains used in each subset.

locations of the pole figure. These grains are a nearly-untwinned grain (white star) and a Dauphiné-twinned grain (black star). In the kinematic reference frame, the Dauphiné-twinned grain plots near the center, and the nearly-untwinned grain plots near the primitive on the lineation (Fig. 8a). CVA analysis indicates that these two grain populations should be plotted in different reference frames, with the Dauphiné-twinned grains and the nearly-untwinned grains plotted in the kinematic and vorticity-normal

reference frames, respectively. Further explanation on the reasoning of this decision is provided in the discussion.

The pole figures showing orientation data of the Dauphiné-twinned (Fig. 8b) and nearly-untwinned grains (Fig. 8c) (see Supplemental Figure SP5 for subset selection) display similar CPOs. In the *c*-axis plot of the Dauphiné-twinned grains, a maximum occurs off-center of the Y-axis and two maxima are located along the primitive circle, at ~60º counterclockwise from the Z-axis; a weak maximum occurs nearly parallel to the Z-axis. The Dauphiné-twinned reference grain plots on the maximum off-center of the Y-axis. In the *c*-axis plot of the nearly-untwinned grains, a maximum occurs off-center of the X-axis and two maxima are located along the primitive circle, at ~60º counterclockwise from the Z-axis. The nearly-untwinned reference grain plots on the maximum off-center of the X-axis.

4.6 Quartz misorientation analysis for the Dauphiné-twinned quartz sample

Misorientation analysis reveals two very different patterns of low-angle misorientation clustering for the two reference grains in soft orientations for prism <a> slip. In the reference grain with extensive Dauphiné twinning, the lowest angle misorientations (3-5º) form clusters about the *c*-axis, *r*-pole, and near the pole to (11-22) (Fig. 9a). At slightly higher values of misorientation (5-10º), there are strong maxima at the *c*-axis and the π-pole, and a weaker maximum near the pole to (20-21). For misorientation angles associated with Dauphiné twinning (55-65º), there is a strong clustering parallel to the *c*-axis. In the nearly-untwinned reference grain, the lowest angle misorientations (3-5º) form clusters about the *c*-axis and *a*-axis (Fig. 9b). At slightly

higher angles of misorientation (5-10º), there is only a strong maximum at the *a*-axis that extends towards the pole to (11-22). Similar to the Dauphiné-twinned reference grain, misorientations from 55-65º strongly cluster about the *c*-axis.

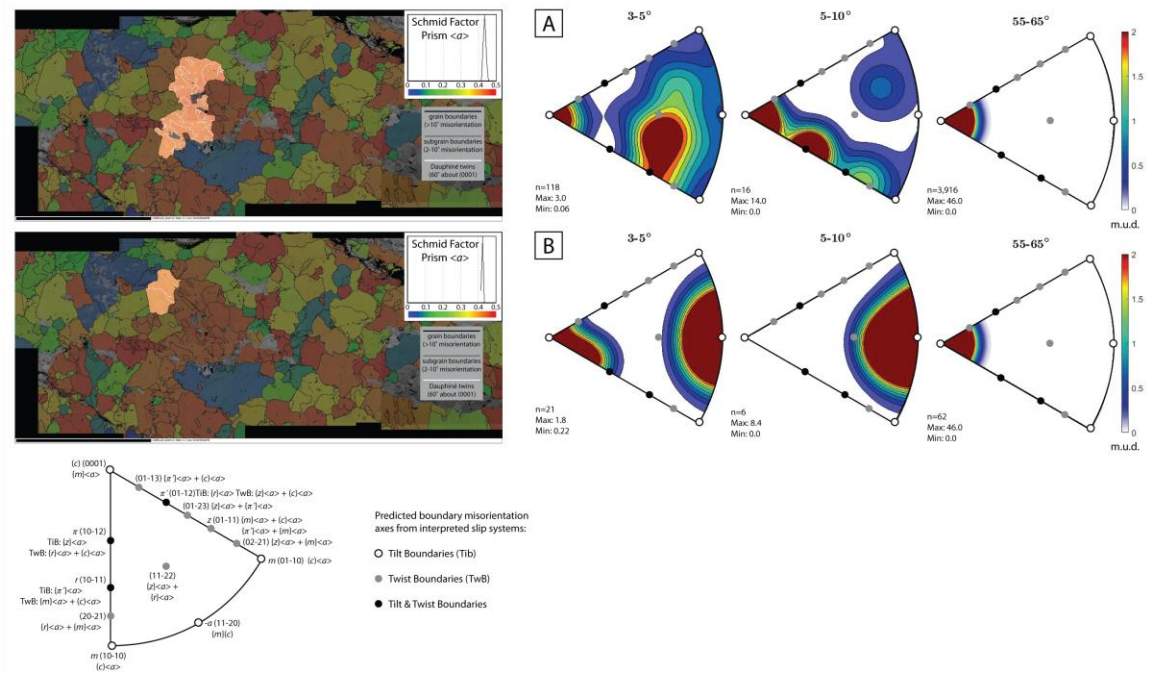

Fig. 9. Misorientation analysis of two reference grains in a soft orientation for prism <*a*> slip. Misorientations are shown in the crystal reference frame, where plots are constructed as contoured upper hemisphere projections with a 10º half width. The number of misorientations (n) and maximum (max) and minimum (min) values of multiples of uniform distribution (m.u.d.) are to the left of each plot. a) The Dauphiné-twinned reference grain is highlighted within the prism <*a*> Schmid factor map, and its misorientation data are shown in contoured plots for misorientation angles 3-5º, 5-10º, and 55-65º. b) The nearly-untwinned reference grain is highlighted within the prism <*a*> Schmid factor map, and its misorientation data are shown in contoured plots for misorientation angles 3-5º, 5-10º, and 55-65º. A key to the inverse pole figure projection for the misorientation data, modified after Lloyd (2004) and Neumann (2000), is shown at the bottom left. The key shows the predicted misorientation axis clustering for slip systems associated with both tilt and twist misorientation boundaries.

Misorientation analysis of all quartz grains in the Dauphiné-twinned quartz sample shows deviations from a random distribution with clusters around crystallographically significant orientation poles. Correlated populations (neighbor-pairs) deviate from random between 3-10º and 55-65º in the misorientation angle distribution histogram, with two distinct low-angle misorientation populations at 3-5º and 5-10º (Fig.

10a). The uncorrelated population (random-pair) closely follows the random distribution curve. Misorientations from 3-5º cluster around the *c*-axis, with subordinate maxima about the π-pole and *a*-axis. Misorientations from 5-10º also cluster about the *c*-axis, but show subordinate maxima about the π'- and *r*-poles, and some spread between the *m*-poles and *a*-axis (Fig. 10b). Misorientations from 55-65º cluster strongly around the pole to the *c*-axis, with weaker clustering around the π- and *z*-poles, and the poles to (11-22) and (20-21) (Fig. 10b).

A subset of Dauphiné-twinned grains (Fig. 10c) shows preferential clustering of misorientations similar to those observed in the analysis of all of the quartz grains. The lowest angle misorientations (3-5º) form clusters about the *c*-axis, and the (01-23) pole, *r*-pole, and π-pole. Low-angle misorientations (5-10º) form a maximum at the *c*-axis and at the π'-pole. For misorientations from 55-65º, there is a strong clustering parallel to the *c*-axis with very weak clusters on the *z*-pole and pole to (11-22).

Misorientations from the subset of Dauphiné twins generally form stronger maxima compared to the subset of Dauphiné-twinned grains with distinctly different clustering patterns (Fig. 10d). Misorientations from 3-5º form a strong maximum at the *c*-axis and a weak maximum near the (11-22) pole with misorientations arcing between the pole to (01-23) and the π-pole, with a stronger maximum on the π-pole. Misorientations from 5-10º cluster at the *c*-axis and on the π- and *m*-poles. Misorientations from 55-65º form a strong maximum on the (11-22) pole.

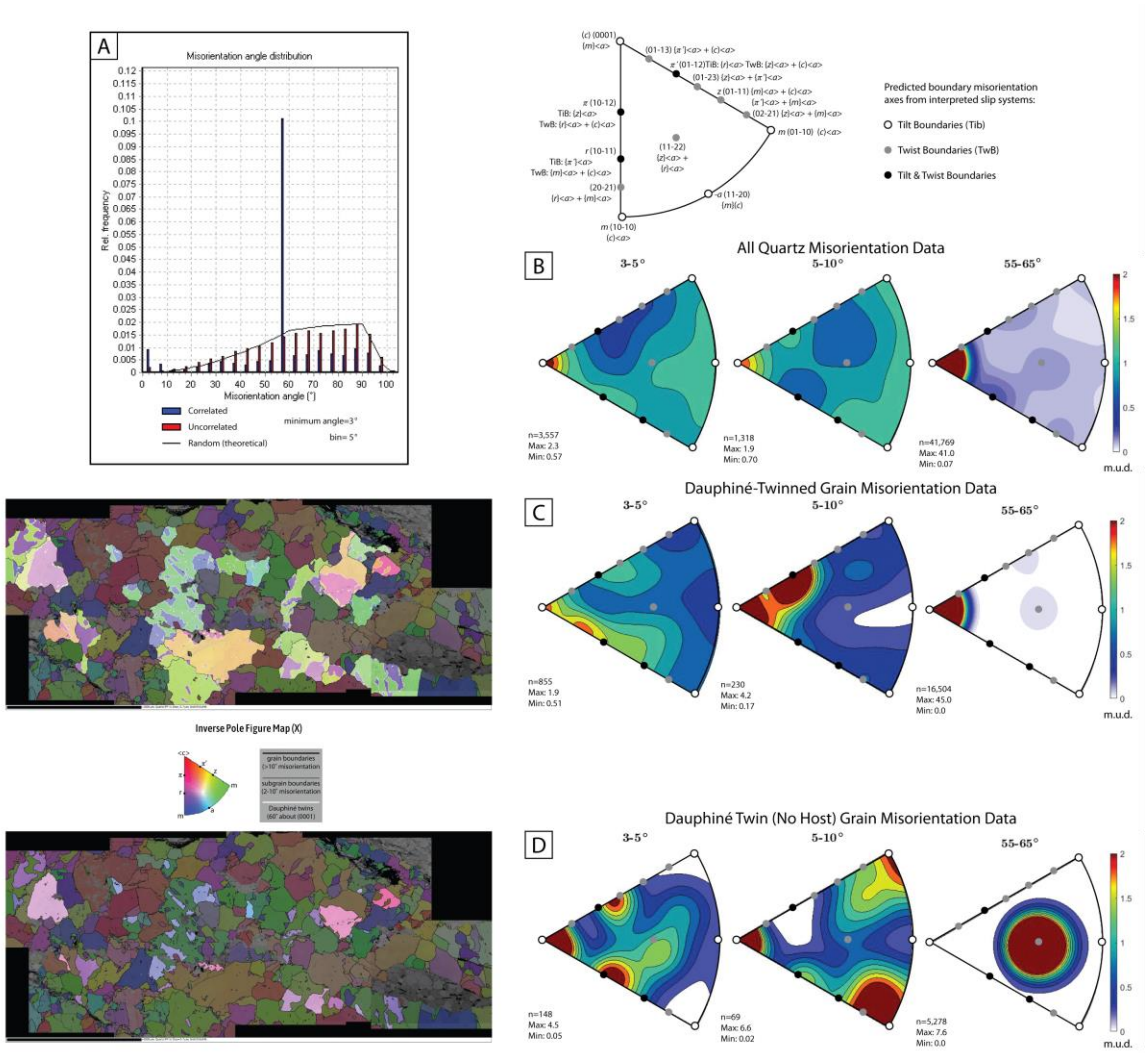

Fig. 10. Misorientation analysis of all quartz grains, Dauphiné-twinned grains, and the Dauphiné twins (*r*-twin) with maps highlighting the grains in each subset. Misorientations are shown in the crystal reference frame, where plots are constructed as contoured upper hemisphere projections with a 10º half width. The number of misorientations (n) and maximum (max) and minimum (min) values of multiples of uniform distribution (m.u.d.) are to the left of each plot. a) The misorientation angle distribution histogram shows correlated (neighbor-pair) and uncorrelated (random-pair) populations relative to a random fabric distribution curve. b) Contoured data for misorientations from all quartz grains from 3-5º, 5-10º, and 55-65º. c) A subset of Dauphiné-twinned grains are highlighted within the IPF-X map, and their misorientation data are shown in contoured plots for misorientations from 3-5º, 5-10º, and 55-65º. d) A subset of Dauphiné twins are highlighted within the IPF-X map, and their misorientation data are shown in contoured plots for misorientations from 3-5º, 5-10º, and 55-65º. A key to the inverse pole figure projection for the misorientation data, modified after Lloyd (2004) and Neumann (2000), is shown at the bottom left. The key shows the predicted misorientation axis clustering for slip systems associated with both tilt and twist misorientation boundaries.

Chapter 5: Discussion

5.1 Microstructural development and dynamic recrystallization

5.1.1 Untwinned quartz sample

Microstructural observations via light microscopy and EBSD indicate crystal plastic deformation of both quartz and plagioclase, where strain is more prominently partitioned into dynamically recrystallized quartz. Plagioclase is extensively recrystallized based on the abundance of fine grains (Fig. 2c) and the rarity of porphyroclasts (Fig. 2d); subgrain development along the rims of porphyroclasts suggests recrystallization by a subgrain rotation (SGR) recrystallization mechanism. In contrast, quartz displays classic GBM microstructures such as lobate grain shapes (Fig. 3a), grain boundary pinning (Figs. 2e, 2f, 3a), and 'island' grains (Fig. 3b), all of which indicate highly mobile grain boundaries. The rapid movement of grain boundaries through grain interiors results in recovery and low intra-grain crystal plasticity (Fig. 3c) (e.g., Hirth and Tullis, 1992; Stipp et al., 2002). Efficient dynamic recrystallization of quartz resulted in strain partitioning into the essentially monomineralic S-fabric domains. We interpret the modally abundant quartz as a rheology-controlling, interconnected network of grains relative to the mixed zones of fine-grained plagioclase and micas that experience phase pinning.

5.1.2 Dauphiné-twinned quartz sample

Microstructural observations indicate crystal plastic deformation of both plagioclase and quartz, but with strain partitioning into quartz that is both dynamically recrystallized and extensively Dauphiné twinned. As with the untwinned quartz sample, plagioclase porphyroclasts are rare; in this sample, some are completely recrystallized,

yet not disaggregated, within quartz domains (Fig. 4d). Though uncommon, the presence of both intact and recrystallized porphyroclasts indicates rheologic competence relative to recrystallized quartz, which makes up the monomineralic S-fabric domains. In the S-fabric domains, quartz displays similar GBM microstructures to the untwinned quartz sample (Figs. 4e, 4f, 5a), and similarly, we interpret quartz as being the rheology-controlling mineral relative to plagioclase porphyroclasts and mixed plagioclase-mica zones. However, the prevalent Dauphiné twinning (Fig. 5a) indicates that deformation is accommodated in quartz in a way that is distinct from the untwinned quartz sample.

The IPF and Schmid factor maps of the Dauphiné-twinned sample reveal some consistency in the orientation of the Dauphiné-twinned grains, which contributes to its distinction from the untwinned quartz sample. In the IPF-X map (Fig. 5b), the dominant green and purple colors of the Dauphiné-twinned grains indicate a preferred orientation where the green host grains and the purple twins within them have their poles to $\{z\}$ and poles to $\{r\}$ oriented parallel to the lineation, respectively. This orientation is consistent with the Dauphiné-twinned grains having their $\{z\}$ and $\{r\}$ planes normal to the foliation, which is contrary to other studies where Dauphiné-twinned grains are observed to have their $\{r\}$ planes oriented parallel to the foliation such that they are at high angles to the direction of maximum principal stress (Menegon et al., 2011; Rahl et al., 2018). The Schmid factor maps (Fig. 7) corroborate this observation, showing that many twinned host grains are not optimally oriented for rhomb $<a>$ slip, though the twinned portions of those grains are in softer orientations for rhomb $<a>$ slip relative to their hosts (Fig. 7b).

Instead, the orthogonal orientation of the rhomb planes {*r*} relative to the trace of foliation in our Dauphiné-twinned sample points to a complicated 3D deformation geometry in the shear zone.

5.2 CVA analysis

The CVA plots show a distinct difference in the deformation geometry for 1) the untwinned and Dauphiné-twinned quartz samples, and 2) the constituent minerals within a given sample. Lineations in the shear zone are neither vertical nor horizontal, therefore we interpret the shear zone to have undergone inclined transpression (Jones et al., 2004). Though we observe changes in the deformation geometry in the samples, the lineations are not changing. As deformation changes from simple shear- to pure shear-dominated, the vorticity axes switch from being normal to and parallel to the stretching lineation, respectively. The bulk CVA plot for the untwinned quartz sample (Fig. 6a) has a maximum that is inconsistent with either pure shear-dominated or simple shear-dominated deformation (Fig. 6). The bulk pattern may be explained by the geometry and relative strength of the CVA patterns of the constituent minerals; plots for muscovite (Fig. 6b) and quartz (Fig. 6c) show that the bulk CVA maximum is most affected by the strong muscovite CVA patterns, and less so by the weaker quartz CVA pattern. In contrast to the untwinned quartz sample, the bulk CVA pattern for the Dauphiné-twinned sample (Fig. 6d) is consistent with pure shear-dominated deformation (Fig. 6). However, the CVA plots for the constituent minerals in the Dauphiné-twinned sample (Fig. 6e, 6f) do not all share this geometry. They are distinct from one another, just as they are in the untwinned quartz sample, suggesting that the 3D deformation geometry is partitioned differently between the minerals in a given sample. However, there are some similarities

in the mineral CVA patterns when comparing the samples: the muscovite and biotite CVAs are similar to each other, suggesting similar behavior of these minerals within the shear zone. The quartz CVA patterns are dramatically different between the samples, indicating that the 3D deformation geometry promotes different behavior of quartz in these otherwise similar samples.

The muscovite and biotite CVA patterns of the untwinned and Dauphiné-twinned quartz samples record pure shear-dominated deformation with spread along the primitive circle. The micas are the weakest phase, which aligns with an experimental study from Holyoke and Tullis (2006) where muscovite was the weakest phase compared to the plagioclase and quartz framework. Therefore, muscovite and biotite record the most recent kinematics. We interpret the spread along the primitive to be a result of grains not be being oriented perfectly parallel to foliation (Figs. 2b, 4b) as a result of the fabric rotating over time. This is due to the complex rotations associated with an inclined-transpressional system, which can give rise to a changing sense of vorticity (Jones et al., 2004). Therefore, the N-S populations (Fig. 6b, 6e) are interpreted to be a result of the changing sense of vorticity and older than the more E-W populations.

The quartz CVA patterns of the untwinned and Dauphiné-twinned quartz samples show a transition from simple shear- to pure shear-dominated deformation, respectively, offering insight into how quartz behavior is different between samples. The quartz CVA pattern in the untwinned quartz sample (Fig. 6c) shows a partial girdle between the CVA patterns associated with simple shear- (Y max) and pure shear-dominated deformation (X max) (Fig. 6). In contrast, the quartz CVA pattern from the Dauphiné-twinned sample (Fig. 6f) has a set of X maxima associated with pure shear-dominated deformation, and

an orthogonal set of maxima that are also on the primitive. The nearly-untwinned grains within this sample correspond to the X maxima, whereas the orthogonal set corresponds to the Dauphiné-twinned grains within the sample. Therefore, the Dauphiné-twinned grains are not deforming in a geometry consistent with pure shear-dominated deformation, which suggests that the Dauphiné-twinned and nearly-untwinned grains represent grain populations that are less and more deformable with pure shear deformation, respectively. We evaluate this interpretation further by close inspection of the Dauphiné-twinned and nearly-untwinned grains in the EBSD maps of the Dauphiné-twinned sample.

The EBSD maps highlight important differences in the deformability of the Dauphiné-twinned and nearly-untwinned grains. The rhomb <*a*> Schmid factor map (Fig. 7b) shows that the *r*-twins in the Dauphiné-twinned grains are commonly red in color, indicating a far softer orientation for slip relative to their host. In some Dauphiné-twinned grains, the red color dominates, indicating that the twin makes up the majority of the grain area. In addition, most of the nearly-untwinned grains are also red in color. We interpret this continuum of microstructures as evidence that twinning has gone to completion in the nearly-untwinned grains, as also documented by (Menegon et al., 2011). The completion of twinning allowed the nearly-untwinned grains to be more deformable based on the isotropic nature of quartz. Therefore, the Dauphiné-twinned grains may represent an earlier microstructure that has been partially overprinted by the growth of the nearly-untwinned grains. Given that the nearly-untwinned grains in this sample are commonly observed to protrude into the Dauphiné-twinned grains (see red and orange grains on either side of starred grain at the top of Fig. 5b), and have lower

GOS (Fig. 5c) and lower density of local misorientations (Fig. 5d) relative to the Dauphiné-twinned grains, we interpret the Dauphiné twinning as an older microstructure relative to the nearly-untwinned grains that impinge upon them. We interpret that the nearly-untwinned quartz in soft orientations for rhomb <*a*>slip could more easily accommodate the change in deformation compared to the less deformable, Dauphiné-twinned quartz grains.

We attribute the differences in the CVA patterns of the nearly-untwinned grains relative to Dauphiné-twinned grains to be a result of the deformability of these grain populations. The Dauphiné-twinned grains have large host areas of the grains having the *z*-plane normal to the lineation (Fig. 5b), which create regions that behave more rigidly compared to the nearly-untwinned grains (Fig. 5c), resulting in the Dauphiné-twinned grain being less responsive to the onset of pure shear-dominated deformation. The *r*-twin, with lower GOS values than the *z*-twin (Fig. 5b,c), is more deformable and easily accommodates the shift to pure shear-dominated deformation as recorded by the CVA pattern.

Our interpretation differs from other studies of Dauphiné-twinned grains (Menegon et al. 2011) in that we apply cross-cutting relations to determine the relative age of the Dauphiné-twinned to the nearly-untwinned grains, and we apply CVA analysis to determine how the deformation geometry of the shear zone has changed. In our study, the Dauphiné-twinned and nearly-untwinned grains reflect the partitioning of simple shear- and pure shear-dominated deformation, respectively, as the shear zone evolved (Fig. 6g). We determine that it is necessary to consider CVA analysis when analyzing grain populations in transpressional shear zones and to look at the CVA for individual

mineral phases. During inclined transpression, both simple shear and pure shear deformation are occurring, and minerals may deform differently as a function of mineral strength. By analyzing the CVA of individual minerals, it can help to determine how deformation has changed through the evolution of the shear zone by determining the deformation geometries preserved in the relatively weaker and stronger minerals. This has important implications for the interpretation of fabrics with multiple deformation events because it can help researchers understand why grains may appear more deformable to the active slip systems in Schmid maps but are actually less deformable due to the orientation of the grains vorticity axis.

5.3 Slip Systems

The two deformation geometries indicated by CVA analysis has implications for how CPO plots are displayed. Grains that show simple shear-dominated deformation should be plotted in the kinematic reference frame while grains that display pure shear-dominated deformation should be plotted in the vorticity normal reference frame (Giorgis et al., 2016). This is most clearly displayed in the *c*-axis pole figure for all of the quartz grains. Clusters indicate predominantly prism <*a*> slip is active, with weaker activation of the rhomb <*a*>, prism [*c*], and basal <*a*> slip systems. The Dauphiné-twinned and nearly-untwinned reference grain plot near the clusters that indicate prism <*a*> and prism [*c*] slip, respectively. The reference grains, though, both show preference for prism <*a*> slip. Therefore, to correctly display the orientation data, the two grain populations of Dauphiné-twinned and nearly-untwinned grains need to be plotted on separate pole figures in their respective reference frames. Furthermore, the cluster indicating prism [*c*] slip is likely overly strong. Both subsets display CPOs that show a loss of a girdle and

narrow maximum that indicates prism <*a*> slip, which is associated with high temperature deformation, along with maxima on the primitive indicating basal <*a*> slip (e.g. Toy et al., 2008). This is consistent with the Schmid factor prism <*a*> map (Fig. 7c) that shows the most grains oriented favorably for slip.

The loss of girdle and narrow prism <*a*> maximum in the c-axis pole figure (Fig. 8) is coincident with the transition to GBM DRX (Stipp et al., 2002; Law, 2014). The narrowing of the prism <*a*> maximum signifies higher temperatures of deformation (Stipp et al., 2002). Though quartz CPO development is not always dependent on temperature and can vary based on strain rate and water weakening (Tullis et al., 1973; Heilbronner and Tullis, 2006; Muto et al., 2011; Law, 2014), the temperature estimates from fabric development are similar with temperatures obtained from Zr in titanite temperature from a nearby sample of 608ºC (Buritica, 2018). We interpret the fabric in the Dauphiné-twinned quartz sample to preserve amphibolite facies conditions with a transition from simple shear- to pure shear-dominated deformation.

Misorientation analysis of the Dauphiné-twinned (Fig. 9b) and nearly-untwinned (Fig. 9c) quartz reference grains in the Dauphiné-twinned sample reveals patterns that are consistent with the activation of known high-temperature slip systems. The misorientations from 5-10º are interpreted to represent an older population compared to the misorientations from 3-5º as the former have accumulated more misorientation. The lowest-angle misorientations (3-5º) in the Dauphiné-twinned grain indicate activation of {*m*}<*a*>, {*π'*}<*a*>, and {*r*}<*a*> + {*z*}<*a*> slip, whereas the slightly higher-angle misorientations (5-10º) indicate the greatest contribution from {*m*}<*a*> and {*z*}<*a*> slip and minor activation of {*r*}<*a*> + {*m*}<*a*> slip (Fig. 9b). All of these slip systems are

known to occur in naturally deformed quartz deforming by dislocation creep at high temperatures (Neumann, 2000; Stipp et al., 2002; Lloyd, 2004; Toy et al., 2008). Lowest-angle misorientations in the nearly-untwinned grain show activation of {*m*}<*a*> and {*m*}[*c*] slip, whereas slightly higher-angle misorientations (5-10º) only indicate activation of {*m*}[*c*] slip. Prism slip systems are particularly correlative with higher temperature deformation (Mainprice et al., 1986; Stipp et al., 2002; Toy et al., 2008).

The misorientation data indicate that prism slip systems (i.e., slip on {*m*} planes) are more common in the nearly-untwinned reference grain compared to the Dauphiné-twinned reference grain, where {*r*}<*a*>, {*z*}<*a*>, and {*π'*}<*a*> slip systems dominate. Previous studies (Lloyd, 2004; Menegon et al., 2011; Rahl et al., 2018) also observe these dominant slip systems to be associated with Dauphiné twins. Though both reference grains appear optimally oriented for {*m*}<*a*> slip as observed in the Schmid map (Fig. 7c), they have different grain orientations (Fig. 5b). The orientation of the Dauphiné-twinned grain and the activity of low-temperature slip systems (i.e. slip on the {*r*} and {*z*} planes) (i.e. Morales et al., 2014) in the Dauphiné-twinned grain (Fig. 9a) results in the grain being less deformable for the deformation conditions and compared to the nearly-untwinned grain (Fig. 9b). This results in strain partitioning between the Dauphiné-twinned and nearly-untwinned grain populations as the deformation changed from simple shear- to pure shear-dominated in the shear zone.

Misorientation analysis of all quartz data confirms both the dynamic recrystallization mechanism and the active slip systems. In the misorientation angle distribution histogram (Fig. 10a), neighbor pair misorientations deviate from random at low angles (<10º), whereas subsequent misorientations follow the random distribution

curve, similar to what is documented for GBM recrystallization in other studies (Neumann, 2000; Wheeler et al., 2001). The misorientations that deviate from random at 55-60º are associated with Dauphiné twins (Lloyd, 2004). Subgrain walls are generally perpendicular to foliation (Fig. 5d) indicating tilt boundaries are expected to be most prevalent (Kruse et al., 2001; Lloyd, 2004), but there are rare subgrain boundaries that are oriented subparallel to foliation, indicating twist boundaries and the occurrence of cross-slip (Lloyd, 2004). Grains with both low angle (<10º) and moderate angle (55-65º) misorientation populations show a preference for {*m*}<*a*> slip over {*r*}<*a*> slip (Fig. 10b). We interpret the difference between the 5-10º misorientation plot where there is clustering about the *π'*-pole and the 3-5º misorientation plot where there is clustering about the *π*-pole as a result of progressive Dauphiné twinning, as twins develop preferentially around the *π*- and *r*-pole (Lloyd, 2004; Wenk et al., 2006). The continued activation of the {*r*}<*a*> and {*z*}<*a*> slip systems associated with twinning acted to keep the Dauphiné-twinned grains less deformable while the {*m*}<*a*> and {*m*}[*c*] slip systems were dominant.

Low angle misorientations (3-10º) from all quartz data indicate weak activation of {*m*}[*c*] slip (Fig. 10b). We conclude that this slip system is associated with the nearly-untwinned quartz grain population that indicates pure shear deformation, as this slip system is also observed in the nearly-untwinned reference grain. Based on the Schmid maps (Fig. 7c,d) and the nearly-untwinned reference grain, the {*m*}<*a*> and {*m*}[*c*] slip systems are associated with the pure shear deformation (Fig. 9b,6g). Though basal <*a*> slip is generally considered a low-temperature slip system (i.e. Morales et al., 2014), Toy et al. (2008) argues that other factors (i.e. strain or water) could affect slip system

activity. We interpret that misorientations from 5-10º are associated with the prism [*c*] slip due to the presence of chessboard extinction (Fig. 4g) (Mainprice et al., 1986; Stipp et al., 2002).

Misorientation analysis of the Dauphiné twin subset (Fig. 10c) reveals similar misorientations with respect to the all quartz subset and the Dauphiné-twinned reference grain. The strongest clusters in the 3-5º misorientations indicate that the {*m*}<*a*> and {*z*}<*a*> slip systems are most active, whereas the weaker clusters indicate subordinate activation of the {*π'*}<*a*>, and {*π'*}<*a*> + {*z*}<*a*> slip systems. The misorientations from 5-10º have stronger clustering than misorientations from 3-5º for {*m*}<*a*> slip with and activity of the {*r*}<*a*> slip system. We interpret the change in misorientation clustering patterns between the 5-10º and 3-5º misorientations to be a result of progressive Dauphiné twinning as twinning goes to completion (Wenk et al., 2006). With respect to the 55-65º misorientations, the strong cluster about the *c*-axis indicates {*m*}<*a*> slip, which is associated with Dauphiné twinning (Lloyd, 2004). The weaker clusters are associated with {*r*}<*a*> + {*z*}<*a*> and {*π'*}<*a*> + {*m*}<*a*> slip systems (e.g. Lloyd, 2004). The different clusters in the 55-65º misorientation plot suggest the presence of both twist- and tilt-type boundaries within the Dauphiné-twinned grains, consistent with Lloyd (2004) where he suggested that Dauphiné twins may be a combination of tilt and twist type boundaries. The continued activation of the {*r*}<*a*>, {*z*}<*a*>, and {*π'*}<*a*> slip systems, as a result of Dauphiné twinning, rendered the Dauphiné-twinned grain population less deformable. This resulted in increased intra-grain strain, particularly in the *z*-twin (Fig. 5b,c), which prevented the Dauphiné-twinned grains from reflecting the change in deformation.

The subset of the *r*-twins in the Dauphiné-twinned grains (Fig. 10d) reveals how the twins more easily recorded the changing deformation of the shear zone interpreted from the CVA (Fig. 6g). The misorientations from 3-5º indicate that the {*m*}<*a*>, {*z*}<*a*>, {*z*}<*a*> + {*π'*}<*a*> slip systems are dominant with minor activation of {*z*}<*a*> + {*r*}<*a*> slip. The misorientations from 5-10º indicate that {*m*}<*a*>, (*c*)<*a*>, and {*r*}<*a*> + {*m*}<*a*> slip are dominant with weaker {*z*}<*a*> slip. The misorientations from 3-5º form an arc between the pole to (01-23) and the *π*-pole. Clusters of misorientations from 5-10º on the *π*-pole both show a preference for the *r*- and *π*-pole, as expected for progressive Dauphiné twinning (Wenk et al., 2006). The difference in misorientations from 3-5º to 5-10º and the stronger clustering around the *π*-pole in misorientations from 3-5º indicates that Dauphiné twinning occurred throughout the deformation history. In the 55-65º plot, the cluster around the (11-22) pole indicates active cross-slip of {*r*} <*a*> + {*z*} <*a*> as twins exchange the {*z*} for the {*r*} direction, which is associated with Dauphiné twinning (Lloyd, 2004; Menegon et al., 2011). Much like the Dauphiné-twinned grains, these slip systems likely kept the *r*-twin less deformable than the nearly-untwinned grains.

The *r*-twins were able to be more deformable than the host (*z*-twin) through the greater activation of the {*m*}<*a*> and (*c*)<*a*> slip systems compared to the Dauphiné-twinned grain subset (Fig. 10d,c). The prism slip systems were most favorable during deformation, and the subset showing *r*-twins has stronger activation of {*m*}<*a*> slip (Fig. 10d) compared to the Dauphiné-twinned grains (Fig. 10c). This indicates that *r*-twins were more deformable compared to the Dauphiné-twinned grains as a whole. The activation of (*c*)<*a*> slip at high temperatures is associated with {*m*}[*c*] (Stipp et al., 2002). We conclude that the (*c*)<*a*> slip system does not result in grains being less

deformable for the high-temperature slip systems, and it was active in conjunction with the {*m*}[*c*] slip system observed in the nearly-untwinned reference grain and all quartz subset. This allowed for the *r*-twin to be more deformable while the high-temperature slip systems were active. The lowest angle misorientations (3-5º) indicate that (*c*)<*a*> slip was no longer active later in the shear zone. This resulted in the twins becoming less deformable to the high-temperature slip systems. The continuous changing sense of vorticity associated with inclined transpression (Jones et al., 2004) caused the shift for where the *r*-twins plotted in the CVA diagram from the E-W position to the N-S position (Fig. 6g) as twins became less deformable due to the active slip systems. The pattern observed in the CVA is similar to what is observed in the micas, where we interpret the N-S populations as older.

5.4 Piezometry

We utilize the Twiss (1977) piezometer to obtain a stress estimate based on grain size piezometry of a recrystallized plagioclase lens contained within the quartz band. Grain sizes of plagioclase are variable (Fig. 11), with a minimum diameter of ~9.35 μm, maximum of ~231.0 μm, and average of ~42.1 μm. These values correspond with stresses of 126.9-136.4, 14.4-15.4, and 45.9-49.1 MPa, respectively. The ranges are associated with a ±5% grain size error based on the percent of indexed points in the EBSD maps (Humphreys, 2001). The highest frequency of the bell curve plots between 30-35 μm, which corresponds with a stress of 53.8-59.7 MPa. We conclude that the stress of 53.8-59.7 MPa best represents the stress conditions as the grain size of 30-35 μm has the highest frequency in the grain size bell curve (Fig. 11). The smallest grain sizes are likely not representative and a result of displaying 3D grains in a 2D EBSD map. The largest

grain size may be part of a not fully recrystallized plagioclase porphyroclast, which is suggested by the presence of subgrain walls and higher intra-grain strain (see Supplemental Fig. SP4). The stress estimate of 53.8-59.7 MPa is similar to observations in experimental studies on quartzite conducted by Stipp and Tullis (2003) that showed the flow stress of 34 MPa was associated with a transition to GBM. The piezometry confirms the conditions of deformation where high temperature and low stress which promoted deformation via GBM DRX.

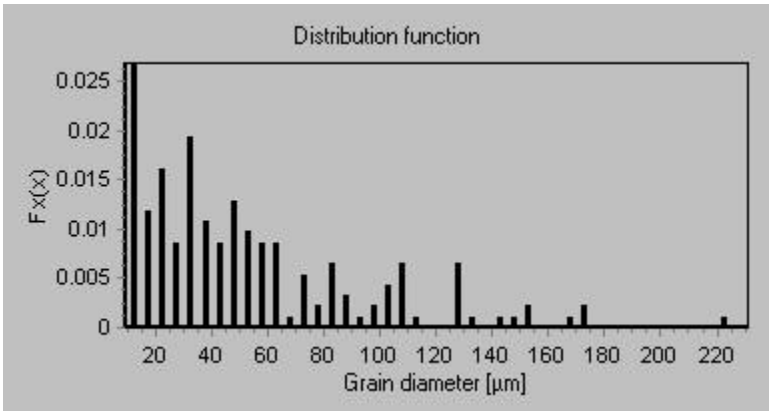

Fig. 11. Grain size histogram of plagioclase contained within the porphyroclast-shaped domain in the Dauphiné-twinned quartz sample binned in 5 µm intervals.

5.5 Strain localization due to Dauphiné twinning and GBM

We conclude that Dauphiné twinning helped to initially localize strain caused by deformation during inclined transpression (Fig. 12a). Mechanical twinning formed as a result of compression and acted to align the *r*- and *z*- poles (Menegon et al., 2011; Rahl et al., 2018). In the thin sections that were cut in the kinematic reference frame (Fig. 12b), the Dauphiné twins' poles appear perpendicular to the shortening direction and parallel to the lineation (Fig. 5b). This contrasts with prior studies where the poles are parallel to the shortening direction (Menegon et al., 2011; Rahl et al., 2018). We conclude that this is a result of the different deformation geometries between our study and prior studies. Menegon et al. (2011) and Rahl et al. (2018) studied samples naturally deformed by

simple shear, whereas our samples deformed in an inclined-transpressional shear zone where both simple shear- and pure shear-dominated deformation occurred (Fig. 6). The grains in our sample were able to rotate and preserve and alignment of the *z*-plane that

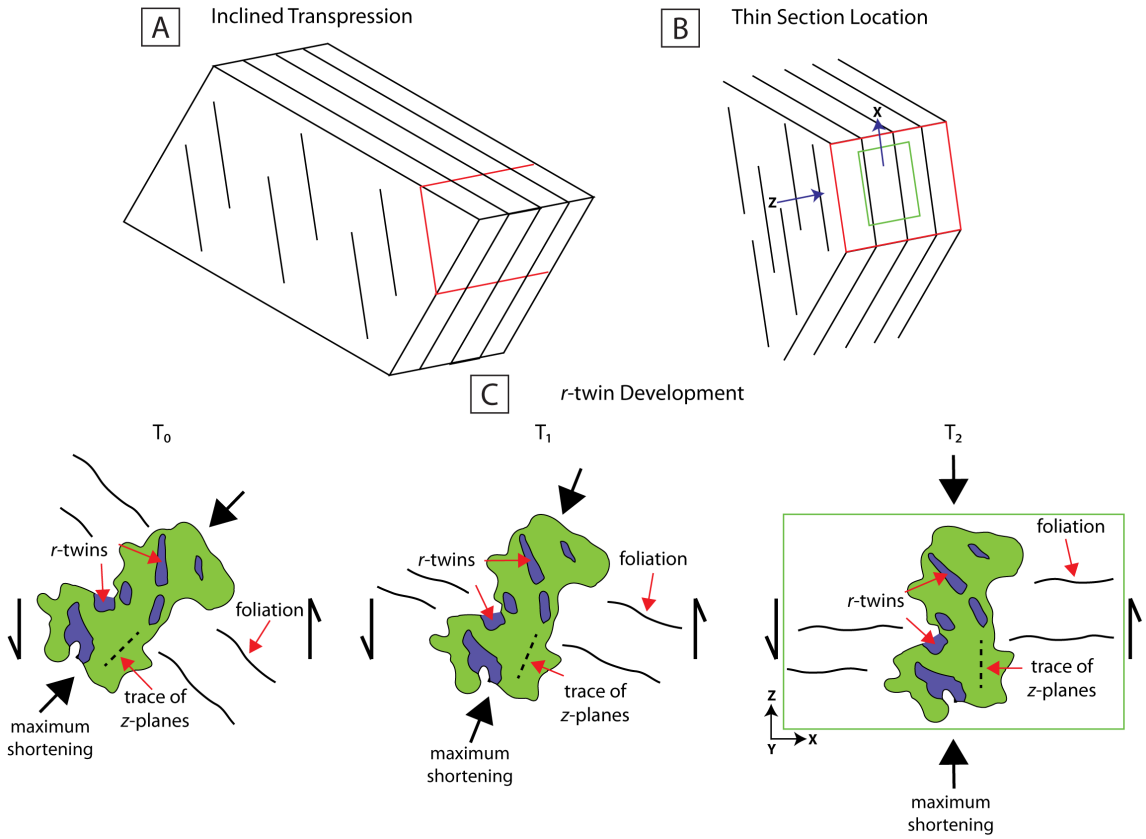

Fig. 12. a) A block diagram showing inclined transpression. The red outline indicates the location of the face in (b). b) Location of the thin section cut in the kinematic reference frame indicated by the green box. The X- and Z-axes are labeled with blue arrows. c) Progressive rotation of the foliation and the Dauphiné-twinned grain showing the orientation of the *z*-planes and *r*-twins to the hypothesized maximum shortening direction during Dauphiné twin formation. Dauphiné twins initially developed while deformation was dominated by simple shear. The interaction of simple shear- and pure shear-dominated deformation promoted grain rotation causing the alignment of the *z*-plane relative to maximum shortening direction to differ from prior studies.

differs from prior studies (Fig. 12c). The formation of Dauphiné twins caused a reduction in grain size, and the contrast in plastic yield between the *r*- and *z*- twins, with the *r*- twin being more deformable, predisposed Dauphiné-twinned grains to strain partitioning and localization (Menegon et al., 2011; Rahl et al., 2018). The *r*-twins were likely a preferred

site for dynamic recrystallization (Stipp and Kunze, 2008; Menegon et al., 2011), specifically GBM DRX, indicated by the lobate nature of the twin boundaries.

GBM DRX in the quartz preserved the large grain size and kept the intra-grain plasticity low (Fig. 5c) by removing high angle boundaries (Platt and Behr, 2011). While quartz underwent GBM DRX, Dauphiné twins developed from GBM (Piazolo et al., 2005). Both the mechanical and GBM-induced Dauphiné twins reduced strain as the more deformable *r*-twins developed (Lloyd, 2004; Menegon et al., 2011; Rahl et al., 2018). We do not interpret Dauphiné twins to be a result of grain retrogression through the α-β phase change (Piazolo et al., 2005) because the temperature of 608±12 ºC (Buritica, 2018) is too low for the transition, which requires temperatures >625 ºC at P=2.5-3.0 kb (Stipp et al., 2002; Wenk et al., 2009). Furthermore, the prograde path through the α-β phase transition would have resulted in the loss of twinning (Wenk et al., 2009) and would have allowed all of the grains to more easily record the changing deformation, which is not observed.

As the shear zone transitioned from simple shear- to pure shear-dominated deformation during inclined transpression, GBM DRX affected the grains' ability to accommodate the changing sense of vorticity. During GBM, migrating grain boundaries sweep through grains, preventing the grains from developing large amounts of intra-grain strain (i.e Stipp et al., 2010). The vorticity axes of grains with Dauphiné twins preserve the simple shear deformation (Fig. 6g). The changing kinematics of deformation could not be accommodated due to higher intra-grain strain (Fig. 5c) and grains being less deformable due to the active slip systems. The nearly-untwinned quartz grains were more deformable based on active slip systems, and GBM DRX kept intra-grain strain low. This

allowed the nearly-untwinned quartz population to record the change in the deformation (Fig. 6c). The more elastic *r*-twin shows the change in the deformation in the CVA plot, reflected in the N-S maxima on the primitive circle (Fig. 6g). However, the stiff *z*-twin portions of the Dauphiné-twinned grains were unable to record this change due to the active slip systems. GBM DRX maintained the relative low intra-grain strain within the grains, thus preserving the CVA pattern associated with the simple shear-dominated deformation.

The Dauphiné-twinned grains preserve low-temperature slip systems (i.e. Morales et al., 2014) resulting in the grain being less deformable for high-temperature deformation (Fig. 9a, 10c). This hindered the grains ability to record the changing deformation. The higher GOS value of the *z*-twin compared to the *r*-twin, as well as the higher GOS value of the Dauphiné-twinned grains compared to the nearly-untwinned grains, drove the mobility of grains with lower intra-grain strain that were more deformable into grains with high intra-grain strain that were less deformable. This is similar what was observed in Little et al. (2015) where poorly oriented grains were preferentially consumed by grains well-oriented for slip during GBM. The mobility of the more deformable grains acted to reduce strain and maintain localization of the shear zone.

Further research should be conducted to compare microscale studies such as this to macroscale studies. In complex kinematic environments, it may be difficult to observe all of the nuances of deformation during field work. Microscale studies provide an opportunity to confirm field observations and capture aspects of shear zone development that cannot be obtained from field work, which allows us to better understand the deformation history. Researchers should conduct continued investigation of this shear

zone to verify its relative crustal level compared to the GMZ exposed along Lake Manapouri (Fig. 1). Other shear zones that developed during the same period of transpression in New Zealand may be interconnected, such as the Indecision Creek Shear Zone (Klepeis et al., 2004; Marcotte et al., 2005) or the Stewart Island Shear Zone (Allibone and Tulloch, 2010). Further work should be done to determine if these shear zones show the same transition of simple shear- to pure shear-dominated deformation during inclined transpression. If these shear zones represent multiple crustal depths, we can further understand strain localization processes and potentially the full evolution of shear zone development through the use of microscale studies.

Chapter 6: Conclusions

Our microstructural, CVA, and EBSD analyses of the untwinned quartz sample and Dauphiné-twinned quartz sample reveal that quartz underwent high-temperature deformation via GBM DRX. We observe a switch in the deformation during inclined transpression in both samples from simple shear- to pure shear-dominated deformation. Muscovite and plagioclase have similar CVA patterns in both samples suggesting similar behavior of these minerals within the shear zone, while quartz CVA patterns dramatically differ between the samples, indicating that the 3D deformation geometry promoted different behavior of the quartz. Nearly-untwinned grains in the Dauphiné-twinned sample records pure shear-dominated deformation while Dauphiné-twinned grains record simple shear-dominated deformation. The difference in deformation geometry is preserved differently between the grain populations based on the deformability of grains due to active slip systems. We apply the Twiss (1977) piezometer to the recrystallized plagioclase which provides a stress value of 53.8-59.7 MPa.

We conclude that the Dauphiné-twinned grains represent and older phase of deformation that was dominated by simple shear. The Dauphiné twins helped to initially localize strain by reducing grain sizes and provided preferred locations for dynamic recrystallization. The shear zone later transitioned to pure shear-dominated deformations as recorded in the micas, nearly-untwinned grains, and *r*-twins. The *r*-twin more easily accommodated the changing geometry of deformation than the *z*-twin due to the *r*-twin being more deformable based on active slip systems. Furthermore, the nearly-untwinned grains are more deformable for deformation than the Dauphiné-twinned grains based on the active slip systems. The preservation of the low-temperature slip systems made the

Dauphiné-twinned grains, particularly the *z*-twin, less deformable and prevented the grains from recording the changes in deformation.

CVA analysis is a powerful technique for examining shear zone development that allows researchers to determine shear zone geometry independent of field measurements. When conducting research of polymineralic rocks, utilizing CVA analysis on individual mineral phases helps to determine how each phase localizes strain differently. By comparing the relative strength of each mineral phase and cross-cutting relationships of grain populations, CVA analysis can indicate how deformation has evolved overtime. Field studies can reveal the macroscale change in geometry, but lacks the ability to identify which portion of deformation each phase records. Microscale studies utilizing CVA analysis can be used to capture aspects of shear zone evolution that cannot be determined from macroscale studies. In our study, the two endmembers of deformation are preserved. This illustrates the complex histories associated with shear zones and how mineral phases act to accommodate the changes in deformation to maintain strain localization.

References:

Allibone, A.H., Jongens, R., Scott, J.M., Tulloch, A.J., Turnbull, I.M., Cooper, A.F., Powell, N.G., Ladley, E.B., King, R.P., and Rattenbury, M.S., 2009, Plutonic rocks of the Median Batholith in eastern and central Fiordland , New Zealand : Field relations , geochemistry , correlation , and nomenclature: New Zealand Journal of Geology and Geophysics, v. 52, p. 101–148, doi: 10.1080/00288300909509882.

Allibone, A.H., and Tulloch, A.J., 2010, Early Cretaceous dextral transpressional deformation within the Median Batholith , Stewart Island , New Zealand: New Zealand Journal of Geology and Geophysics, v. 51, p. 115–134, doi: 10.1080/00288300809509854.

Bachmann, F., Hielscher, R., and Schaeben, H., 2011, Ultramicroscopy Grain detection from 2d and 3d EBSD data — Specification of the MTEX algorithm: Ultramicroscopy, v. 111, p. 1720–1733, doi: 10.1016/j.ultramic.2011.08.002.

Bunge, H.-J., 1982, Texture Analysis in Materials Science: Mathematical Methods: Buttersworth, London.

Buritica, L., 2018, Temporal and Spatial Variations in Magmatism and Transpressional Deformation in the Middle to Lower-Crust of a Cretaceous Arc, Median Batholith, Fiordland, New Zealand, MSc Thesis: CSU-Northridge.

Cross, A.J., Prior, D.J., Stipp, M., and Kidder, S., 2017, The Recrystallized Grain Size Piezometer for Quartz : An EBSD-based calibration: Geophysical Research Letters, v. 44, p. 6667–6674, doi: 10.1002/2017GL073836.

Giorgis, S., Michels, Z., Dair, L., Braudy, N., and Tikoff, B., 2016, Kinematic and vorticity analyses of the western Idaho shear zone , USA: Lithosphere, v. 9, p. 223–234, doi: 10.1130/L518.1.

Heilbronner, R., and Tullis, J., 2006, Evolution of c axis pole figures and grain size during dynamic recrystallization : Results from experimentally sheared quartzite: Geophysi, v. 111, p. 1–19, doi: 10.1029/2005JB004194.

Hirth, G., and Tullis, J.A.N., 1992, Dislocation creep regimes in quartz aggregates: Journal of Structural Geology, v. 14, p. 145–159.

Holyoke, C.W., and Tullis, J., 2006, The interaction between reaction and deformation : an experimental study using a biotite + plagioclase + quartz gneiss: Journal of Metamorphic Geology, v. 24, p. 743–762, doi: 10.1111/j.1525-1314.2006.00666.x.

Humphreys, F.J., 2001, Review Grain and subgrain characterisation by electron backscatter diffraction: Journal of Materials Science, v. 35, p. 3833–3854, doi: 10.1023/A:1017973432592.

Jones, R.R., Holdsworth, R.E., Clegg, P., Mccaffrey, K., and Tavarnelli, E., 2004, Inclined transpression: Journal of Structural Geology, v. 26, p. 1531–1548, doi: 10.1016/j.jsg.2004.01.004.

Klepeis, K.A., Clarke, G.L., Gehrels, G., and Vervoort, J., 2004, Processes controlling

vertical coupling and decoupling between the upper and lower crust of orogens: Results from Fiordland, New Zealand: Journal of Structural Geology, v. 26, p. 765–791, doi: 10.1016/j.jsg.2003.08.012.

Klepeis, K.A., Schwartz, J., Stowell, H., and Tulloch, A., 2016, Gneiss domes, vertical and horizontal mass transfer, and the initiation of extension in the hot lower-crustal root of a continental arc, Fiordland, New Zealand: Lithosphere, v. 8, doi: 10.1130/L490.1.

Kruse, R., Stunitz, H., and Kunze, K., 2001, Dynamic recrystallization processes in plagioclase porphyroclasts: Structural Geology, v. 23, p. 1781–1802.

Law, R.D., 2014, Deformation thermometry based on quartz c -axis fabrics and recrystallization microstructures : A review: Journal of Structural Geology, v. 66, p. 129–161, doi: 10.1016/j.jsg.2014.05.023.

Little, T.A., Prior, D.J., Toy, V.G., and Lindroos, Z.R., 2015, The link between strength of lattice preferred orientation, second phase content and grain boundary migration: A case study from the Alpine Fault zone, New Zealand: Journal of Structural Geology, v. 81, p. 59–77, doi: 10.1016/j.jsg.2015.09.004.

Lloyd, G.E., 2004, Microstructural evolution in a mylonitic quartz simple shear zone: the significant roles of dauphine twinning and misorientation: Geological Society, London, Special Publications, v. 224, p. 39–61.

Mainprice, D., Bouchez, J.-L., Blumenfeld, P., and Tubia, J.M., 1986, Dominant c slip in naturally deformed quartz : Implications for dramatic plastic softening at high temperature: Geology, v. 14, p. 819–822.

Marcotte, S.B., Klepeis, K.A., Clarke, G.L., Gehrels, G., and Hollis, J.A., 2005, Intra-arc transpression in the lower crust and its relationship to magmatism in a Mesozoic magmatic arc: Tectonophysics, v. 407, p. 135–163, doi: 10.1016/j.tecto.2005.07.007.

Menegon, L., Piazolo, S., and Pennacchioni, G., 2011, The effect of Dauphine´ twinning on plastic strain in quartz: , p. 635–652, doi: 10.1007/s00410-010-0554-7.

Michels, Z.D., Kruckenberg, S.C., Davis, J.R., and Tikoff, B., 2015, Determining vorticity axes from grain-scale dispersion of crystallographic orientations: Geology, v. 43, p. 803–806, doi: 10.1130/G36868.1.

Morales, L.F.G., Lloyd, G.E., and Mainprice, D., 2014, Tectonophysics Fabric transitions in quartz via viscoplastic self-consistent modeling part I : Axial compression and simple shear under constant strain: Tectonophysics, v. 636, p. 52–69, doi: 10.1016/j.tecto.2014.08.011.

Morales, L.F.G., Mainprice, D., Lloyd, G.E., Law, R.D., and Euge, P., 2015, Crystal fabric development and slip systems in a quartz mylonite : an approach via transmission electron microscopy and viscoplastic self-consistent modelling: , p. 151–174.

Mortimer, N., Tulloch, A.J., Spark, R.N., Walker, N.W., Ladley, E., Allibone, A., and

Kimbrough, D.L., 1999, Overview of the Median Batholith, New Zealand : a new interpretation of the geology of the Median Tectonic Zone and adjacent rocks: v. 29, p. 257–268.

Muto, J., Hirth, G., Heilbronner, R., and Tullis, J., 2011, Plastic anisotropy and fabric evolution in sheared and recrystallized quartz single crystals: Geophysical Research, v. 116, p. 1–18, doi: 10.1029/2010JB007891.

Neumann, B., 2000, Texture development of recrystallised quartz polycrystals unravelled by orientation and misorientation characteristics: Structural Geology, v. 22, p. 1695–1711.

Pehl, J., and Wenk, H.-R., 2005, Evidence for regional Dauphine twinning in quartz from the Santa Rosa mylonite zone in Southern California. A neutron diffraction study: Journal of Structural Geology, v. 27, p. 1741–1749, doi: 10.1016/j.jsg.2005.06.008.

Piazolo, S., Prior, D.J., and Holness, M.D., 2005, The use of combined cathodoluminescence and EBSD analysis : a case study investigating grain boundary migration mechanisms in quartz: Journal of Microscopy, v. 217, p. 152–161.

Platt, J.P., and Behr, W.M., 2011, Grainsize evolution in ductile shear zones : Implications for strain localization and the strength of the lithosphere: Journal of Structural Geology, v. 33, p. 537–550, doi: 10.1016/j.jsg.2011.01.018.

Prior, D.J., Boyle, A.P., Brenker, F., Cheadle, M.C., Day, A., Lopez, G., Peruzzo, L., Potts, G.J., Reddy, S., Spiess, R., Timms, N. ick E., Trimby, P., Wheeler, J., and Zetterström, L., 1999, The application of electron backscatter diffraction and orientation contrast imaging in the SEM to textural problems in rocks: American Mineralogist, v. 84, p. 1741–1759.

Rahl, J.M., Mcgrew, A.J., Fox, J.A., Latham, J.R., and Gabrielson, T., 2018, Rhomb-dominated crystallographic preferred orientations in incipiently deformed quartz sandstones : A potential paleostress indicator for quartz-rich rocks: v. 46, p. 195–198.

Rattenbury, M., and Isaac, M., 2012, The QMAP 1:250 000 Geological Map of New Zealand project: New Zealand Journal of Geology and Geophysics, v. 55, p. 393–405, doi: 10 .1080 /00288306 .2012 .725417.

Ringwood, M., 2018, Temporal and Spatial Patterns in a Mesozoic Magmatic Arc: Insights from Fiordland, New Zealand: CSU-Northridge.

Schwartz, J.J., Klepeis, K.A., Sadorski, J.F., Stowell, H.H., Tulloch, A.J., and Coble, M.A., 2017, The tempo of continental arc construction in the Mesozoic Median Batholith, Fiordland, New Zealand: Lithosphere, p. L610.1, doi: 10.1130/L610.1.

Scott, J.M., 2013, A review of the location and significance of the boundary between the Western Province and Eastern Province , New Zealand: New Zealand Journal of Geology and Geophysics, v. 56, p. 276–293, doi: 10.1080/00288306.2013.812971.

Scott, J.M., Cooper, A.F., Tulloch, A.J., and Spell, T.L., 2011, Crustal thickening of the Early Cretaceous paleo-Pacific Gondwana margin: Gondwana Research, v. 20, p.

380–394, doi: 10.1016/j.gr.2010.10.008.

Scott, J.M., Palin, J.M., Cooper, A.F., and King, R.P., 2009, Polymetamorphism , zircon growth and retention of early assemblages through the dynamic evolution of a continental arc in Fiordland , New Zealand: Journal of Metamorphic Geology, v. 27, p. 281–294, doi: 10.1111/j.1525-1314.2009.00817.x.

Skemer, P., Katayama, I., Jiang, Z., and Karato, S., 2005, The misorientation index : Development of a new method for calculating the strength of lattice-preferred orientation: v. 411, p. 157–167, doi: 10.1016/j.tecto.2005.08.023.

Stipp, M., and Kunze, K., 2008, Dynamic recrystallization near the brittle-plastic transition in naturally and experimentally deformed quartz aggregates: v. 448, p. 77–97, doi: 10.1016/j.tecto.2007.11.041.

Stipp, M., Stunitz, H., Heilbronner, R., and Schmid, S.M., 2002, The eastern Tonale fault zone : a “natural laboratory” for crystal plastic deformation of quartz over a temperature range from 250 to 700 8 C: Structural Geology, v. 24, p. 1861–1884.

Stipp, M., and Tullis, J., 2003, The recrystallized grain size piezometer for quartz The recrystallized grain size piezometer for quartz: Geophysical Research Letters, v. 30, doi: 10.1029/2003GL018444.

Stipp, M., Tullis, J., Scherwath, M., and Behrmann, J.H., 2010, A new perspective on paleopiezometry : Dynamically recrystallized grain size distributions indicate mechanism changes: Geology, v. 38, p. 759–762, doi: 10.1130/G31162.1.

Thomas, L.A., and Wooster, W.A., 1951, Piezocrescence-The Growth of Dauphine Twinning in Quartz under Stress: Proceedings of the Royal Society of London A: Mathematical, Physical, and Engineering Sciences, v. 208, p. 43–62, doi: 10.1098/rspa.1951.0143.

Toy, V.G., Prior, D.J., and Norris, R.J., 2008, Quartz fabrics in the Alpine Fault mylonites : Influence of pre-existing preferred orientations on fabric development during progressive uplift: Structural Geology, v. 30, p. 602–621, doi: 10.1016/j.jsg.2008.01.001.

Tullis, J., Christie, J.M., and Griggs, D.T., 1973, Microstructures and Preferred Orientations of Experimentally Deformed Quartzites: Geological Society of America Bulletin, v. 84, p. 297–314.

Tullis, J., and Tullis, T., 1972, Preferred Orientation of Quartz Produced by Mechanical Dauphiné Twinning: Thermodynamics and Axial Experiments (H. C. Heard, I. Y. Borg, N. I. Carter, & C. B. Raleigh, Eds.): Flow and Facture of Rocks, Geophysical Monograph Series, v. 16, p. 67–82.

Twiss, B.R.J., 1977, Theory and Applicability of a Recrystallized Grain Size Paleopiezometer, *in* Stress in the Earth, Birkhäuser Basel, Basel, v. 115, p. 227–244.

Wenk, H., Barton, N., Bortolotti, M., Vogel, S.C., Voltolini, M., Lloyd, G.E., and Gonzalez, G.B., 2009, Dauphine´ twinning and texture memory in polycrystalline quartz. Part 3: texture memory during phase transformation: Physics and Chemistry

of Minerals, v. 36, p. 567–583, doi: 10.1007/s00269-009-0302-6.

Wenk, H.-R., Bortolotti, M., Barton, N., Oliver, E., and Brown, D., 2007, Dauphine twinning and texture memory in polycrystalline quartz. Part 2 : In situ neutron diffraction compression experiments: Physics and Chemistry of Minerals, v. 34, p. 599–607, doi: 10.1007/s00269-007-0174-6.

Wenk, H.-R., Rybacki, E., Dresen, G., Lonardelli, I., Barton, N., Hermann, F., and Gonzalez, G., 2006, Dauphine twinning and texture memory in polycrystalline quartz. Part 1 : Experimental deformation of novaculite: Physics and Chemistry of Minerals, v. 33, p. 667–676, doi: 10.1007/s00269-006-0115-9.

Wheeler, J., Prior, D.J., Jiang, Z., R., S., and Trimby, P.W., 2001, The petrological signifcance of misorientations between grains: Contributions to Mineralogy and Petrology, v. 141, p. 109–124, doi: 10.1007/s004100000225.

Appendix A: Hand samples, thin section scans, plagioclase lens, and CPO subsets

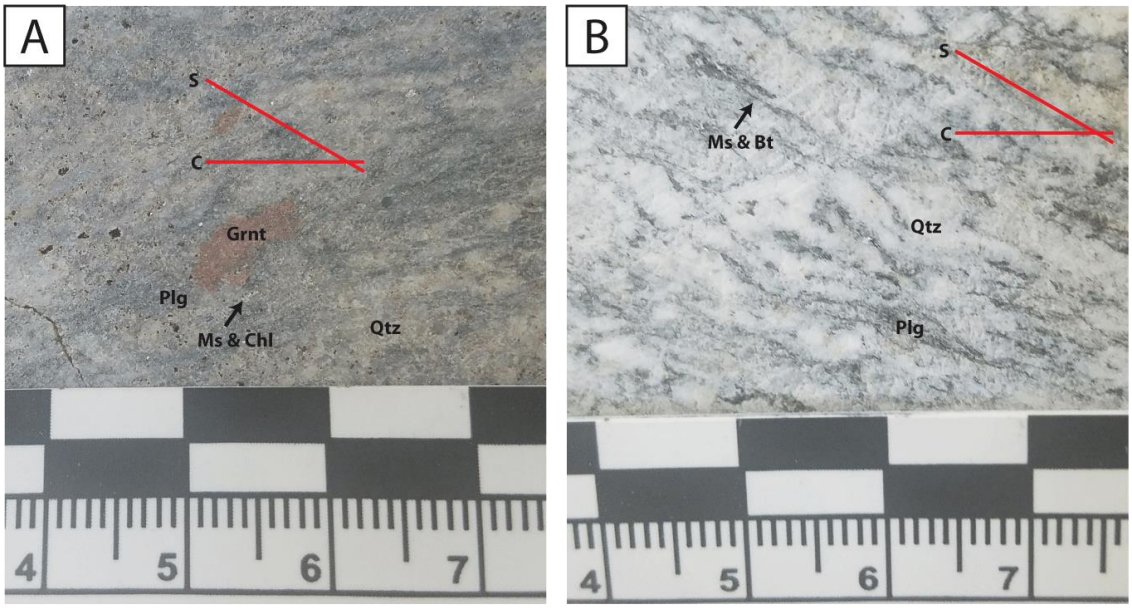

Photo 1A&B. Hand samples of 17NZ41B (a), a muscovite granodiorite with garnet and 17NZ42 (b), a muscovite biotite tonalite. Both samples show S-C mylonitic fabric development on the hand sample scale showing typical development of S-C mylonitic fabric. Sinistral shear sense indicators are observed correlated with top to the west normal sense of movement in the high strain zones.

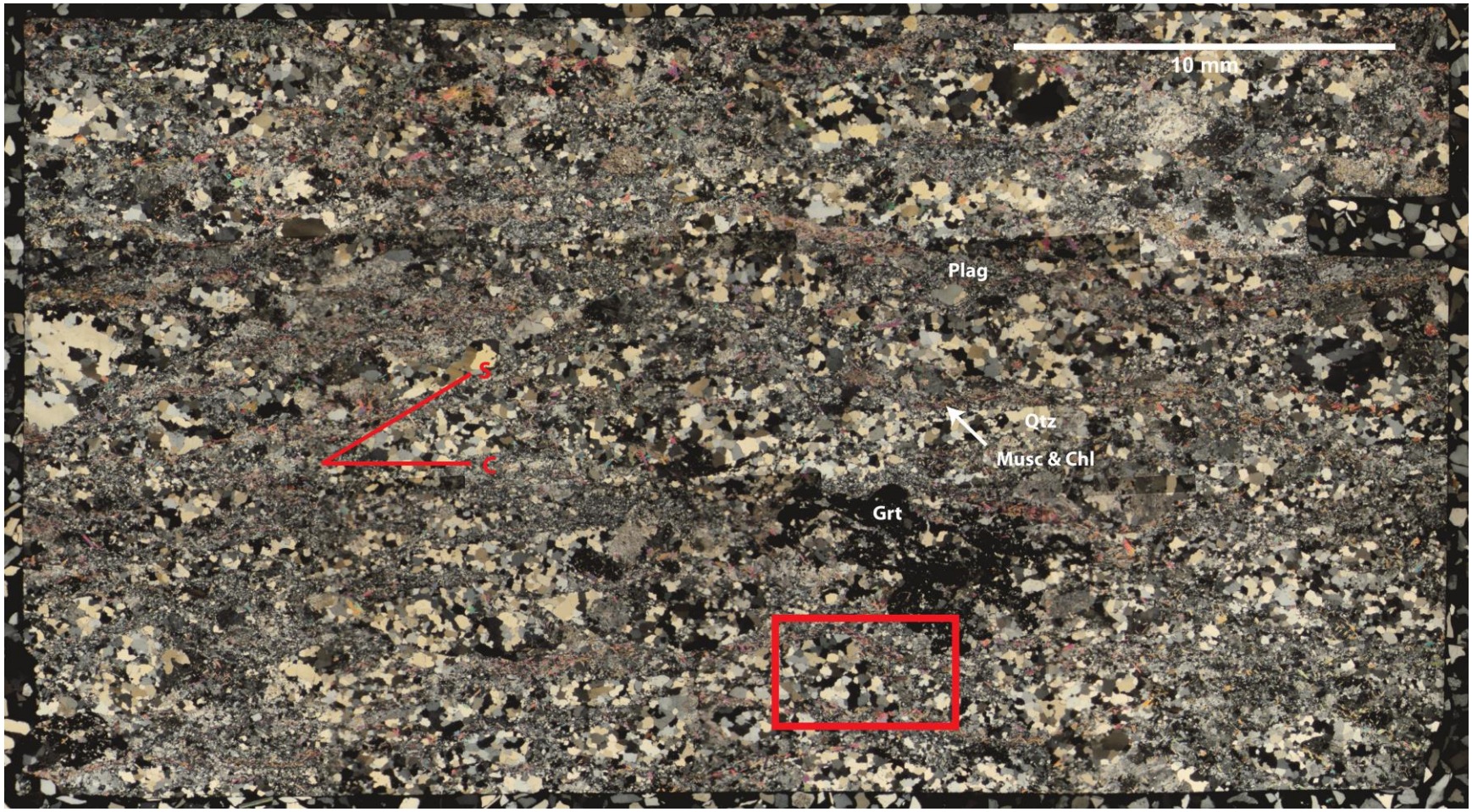

Photo 2. Photomicrograph of sample 17NZ41B in cross-polarized light showing characteristic fabric with coarse grained quartz and fine grained plagioclase in separate bands and irregular shape of garnet. The compositional foliation is defined by layering of muscovite and chlorite at the interface between quartz- and plagioclase-rich bands. *S*-C fabric development is shown in red where muscovite and chlorite align with C-fabric development and quartz aligns with the S-fabric. The red box indicates the targeted area for EBSD analysis where two maps were collected, one of the quartz band and one of a plagioclase porphyroclast near the garnet. Qtz=quartz, Plag=plagioclase, Grt=Garnet, Musc-Muscovite, Chl=Chlorite

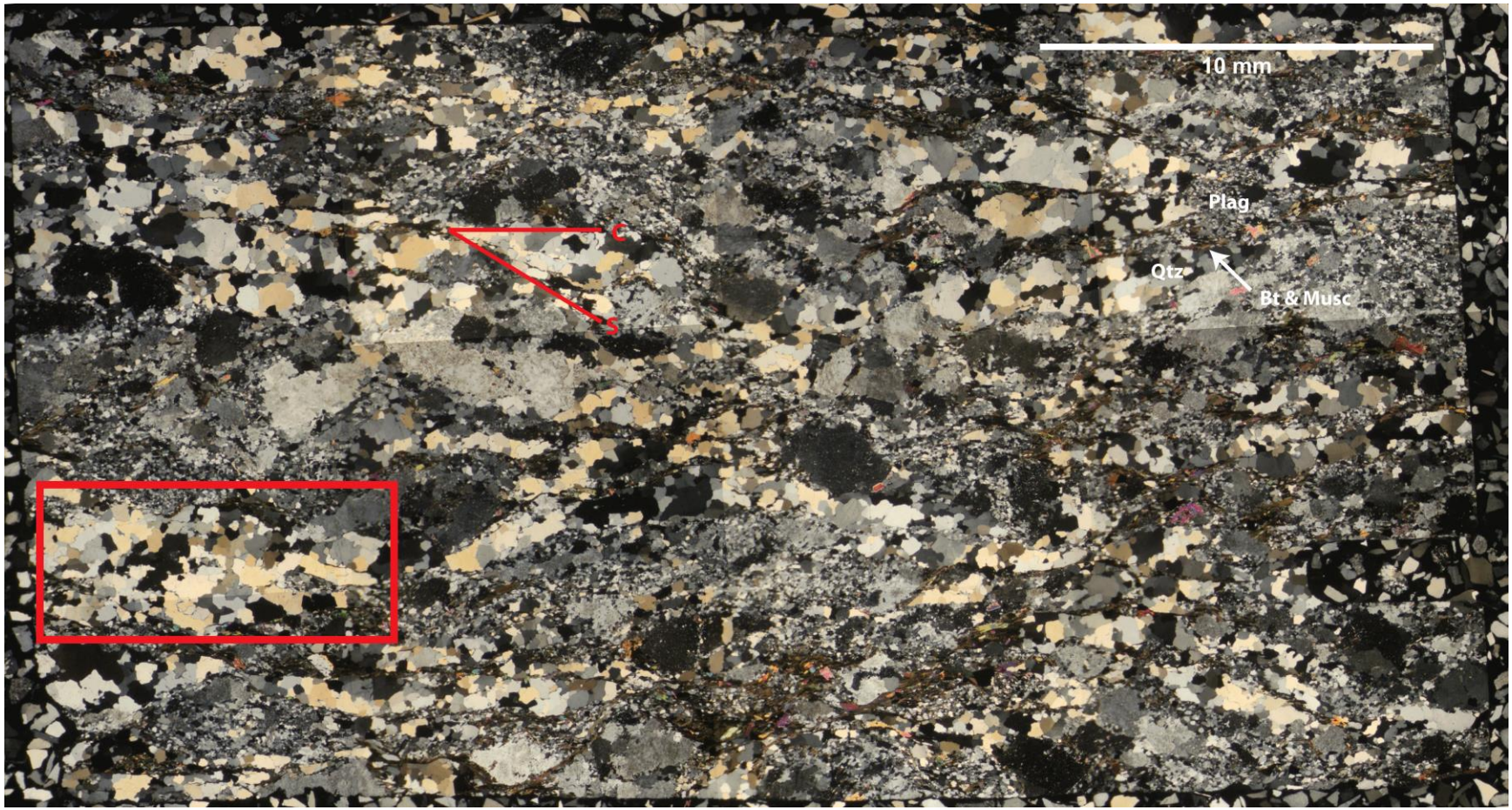

Photo 3. Photomicrograph of sample 17NZ42 in cross-polarized light showing characteristic fabric with coarse grained quartz and fine grained plagioclase in separate bands. The compositional foliation is defined by layering of biotite and muscovite at the interface between quartz- and plagioclase-rich bands. *S*-C fabric development is shown in red where biotite and muscovite define the C-fabric and quartz defines the S-fabric. The red box indicates the targeted area for EBSD analysis. Qtz=Quartz, Plag=Plagioclase, Bt=Biotoite, Musc=Muscovite

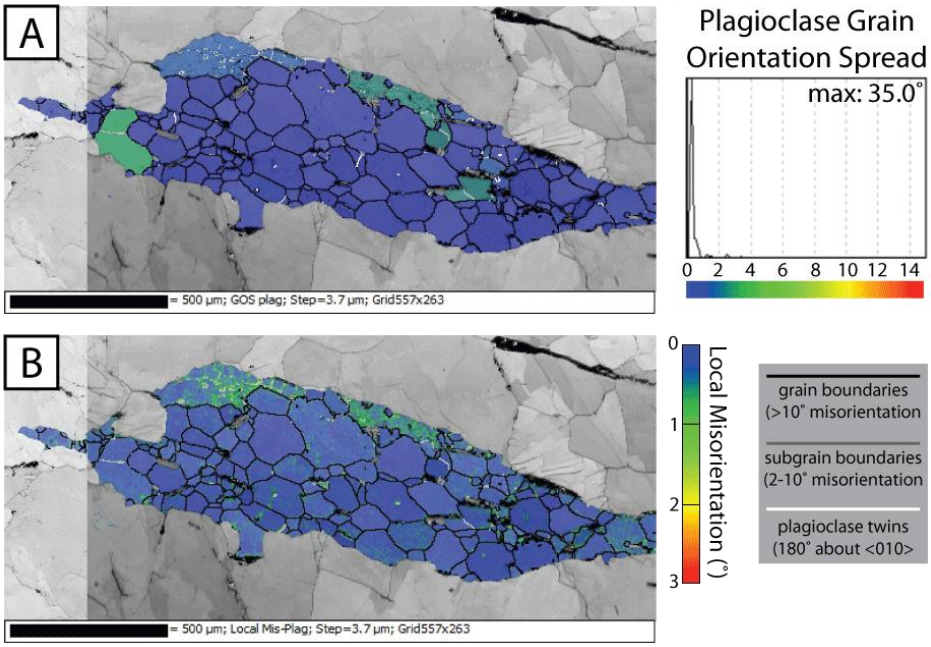

Supplemental Fig. SP4. EBSD maps of recrystallized plagioclase grains within a quartz band (see Figure 6a for phase map) in the Dauphiné-twinned sample. a) GOS map shows grains containing subgrain walls have higher intra-grain crystal plasticity than the surrounding grains. b) Local misorientation map that highlights the substructure developed in the plagioclase grains in contact with quartz.

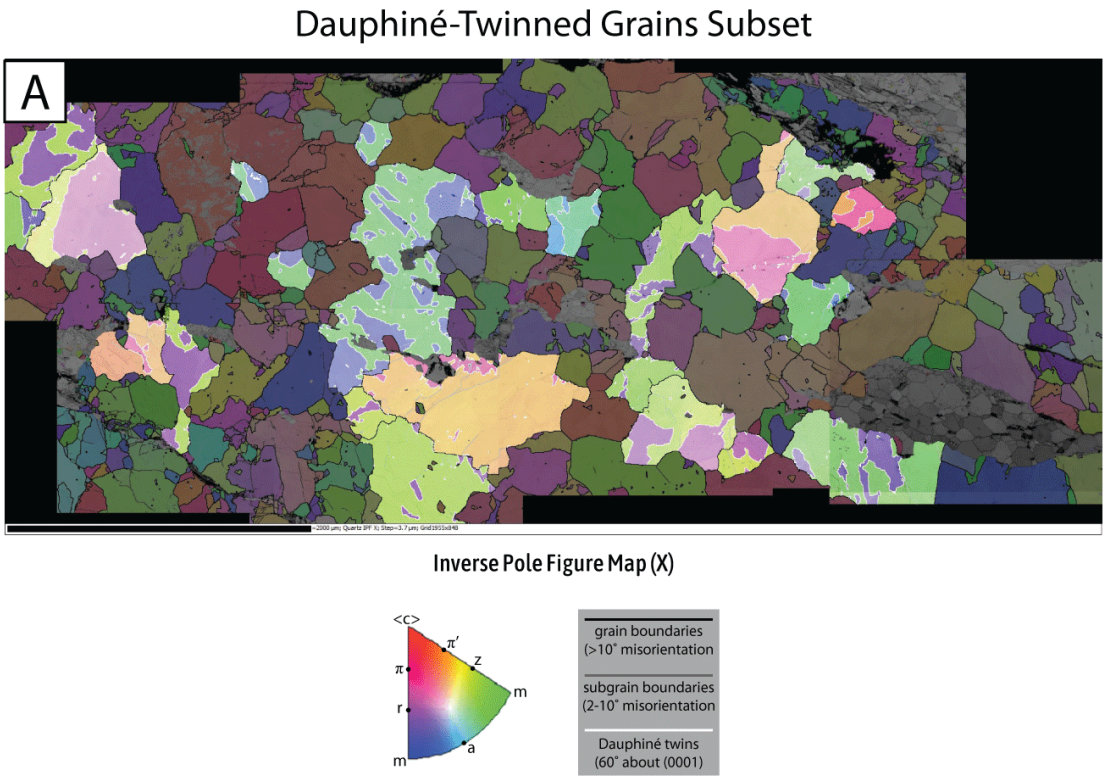

Supplemental Fig. SP5. EBSD maps showing (a) the Dauphiné-twinned grains subset and (b) the nearly-untwinned grains subset selected for generating pole figures in Figure 8.